Journal Pre-proof

Electron spin resonance (ESR), optically stimulated luminescence (OSL) and terrestrial cosmogenic radionuclide (TCN) datingof quartz from a Plio-Pleistocene sandy formation in the Campine area, NE Belgium

Koen Beerten, Koen Verbeeck, Eric Laloy, Veerle Vanacker, Dimitri Vandenberghe, Marcus Christl, Johan De Grave, Laurent Wouters

PII: S1040-6182(20)30323-2

DOI: https://doi.org/10.1016/j.quaint.2020.06.011

Reference: JQI 8347

To appear in: *Quaternary International*

Received Date: 18 June 2019

Revised Date: 5 June 2020

Accepted Date: 10 June 2020

Electron spin resonance (ESR), optically stimulated luminescence (OSL) and terrestrial cosmogenic radionuclide (TCN) datingof quartz from a Plio-Pleistocene sandy formation in the Campine area, NE Belgium

Koen Beerten[a,*], Koen Verbeeck[b], Eric Laloy[a], Veerle Vanacker[c], Dimitri Vandenberghe[d], Marcus Christl[e], Johan De Grave[d], Laurent Wouters[f]

[a] Belgian Nuclear Research Centre (SCK•CEN), Engineered and Geosystems Analysis, Boeretang 200, 2400 Mol, Belgium

[b] Royal Observatory of Belgium, Seismology and Gravimetry Department, Avenue Circulaire 3, 1180 Brussels, Belgium

[c] Georges Lemaitre Centre for Earth and Climate Research, Earth and Life Institute, Université catholique de Louvain, Louvain-la-Neuve, 1348, Belgium

[d] Laboratory of Mineralogy and Petrology, Department of Geology, Ghent University, Krijgslaan 281 (S8), 9000 Gent, Belgium

[e] Laboratory of Ion Beam Physics, ETH-Zurich, Zurich, 8093, Switzerland

[f] Belgian National Agency for Radioactive Waste and enriched Fissile Material (NIRAS/ONDRAF), Long-term Management Department, Avenue des Arts 14, 1210 Brussels, Belgium

*corresponding author kbeerten@sckcen.be

Abstract

The chronostratigraphy of the typical quartz-rich white sands that are intensively quarried in the Campine area, northeastern Belgium, is poorly constrained. In the absence of biostratigraphical data, the age of the deposits, traditionally assigned to the Mol Formation, is thought to be late Pliocene based on sequence stratigraphical correlations (ca. 2.6-3.6 Ma). In an attempt to verify this age, we used a multi-dating method approach on two carefully selected samples in a palaeoseismological trench where the sediment was found to be vertically displaced by the Rauw fault. Three dating methods were used: electron spin resonance (ESR) dating, optically stimulated luminescence (OSL) dating and cosmogenic radionuclide (CRN) dating. In all three cases quartz was found to be a suitable dating material in terms of material properties. However, the ESR dating results based on Ti, Ti-Li and Al centres show strong internal inconsistencies, which can be explained by incomplete bleaching. As such, the youngest ESR ages obtained (ca. 5 Ma) are regarded as an absolute maximum age. In contrast, the OSL ages of ca. 1.5 Ma seem to underestimate the sequence stratigraphical age. The surface exposure CRN dating method using Bayesian inversion suggests that a palaeosurface developed around 1.55 ± 0.80 Ma, and eroded at a rate of ca. 15 m/Ma. Erosion probably accelerated after ca. 0.5-1 Ma and posterior to the last major movement along the Rauw fault.

Keywords

ESR dating; OSL dating; CRN dating; Bayesian inversion; ^{26}Al; ^{10}Be; Pleistocene, erosion rate

1 Introduction

The Mol Formation plays a key role in unravelling the geological history of the border area between the Netherlands, Belgium and Germany (Figure 1). The formation is affected by dormant and active Roer Valley Graben faults, such that its exact chronostratigraphic position would greatly help in determining the seismological history of the area (Vanneste et al., 2013; Verbeeck et al., 2017). Furthermore, the formation records the marine-terrestrial transition in this area as it is thought to have been deposited in a fluvio-estuarine environment during the late Pliocene (Laga et al., 2001; Vandenberghe et al., 2004). Finally, its top surface also records a major post-depositional erosion phase as the Kleine Nete catchment (Scheldt Basin) partially developed where the formation is outcropping (Beerten et al., 2013). A typical feature of the Mol Formation is its very high quartz content, for which reasons it is intensively quarried in northeastern Belgium (Gullentops and Wouters, 1996).

Determining an absolute burial age for sediments older than several 100 ka remains a challenge for the trapped charge dating community. So far, there is no widely accepted dating protocol that can routinely be used to date geological events that reach back to the late Pliocene and Early Quaternary. One possible way to tackle this problem is to apply a multi-dating method scheme, where several preferably independent dating methods are used to establish an age for the event of interest (e.g., Rixhon et al., 2017). First, electron spin resonance (ESR) dating is a good candidate to determine the burial age of Plio-Pleistocene sediment, given the paramagnetic defects involved, typically showing non-saturating behaviour even at high doses (Schellmann et al., 2008). The drawback of the method is the slow bleaching rate of the ESR signals, especially in comparison with optically stimulated luminescence (OSL) dating. Second, OSL dating of quartz using the single aliquot regenerative (SAR) dose protocol is a useful tool to determine the age of the sediments involved here (Rhodes, 2011), given the quartz-rich nature of the Mol Formation, the complete absence of feldspar and the supposedly extremely low dose rate. Finally, cosmogenic radionuclide (CRN) dating has proven to be a useful tool to determine surface and burial ages in the 1 Ma range and beyond, as well as the associated post-depositional erosion rate (Gosse and Klein, 2015).

Recently, the faulted top layers of the Mol Formation were studied in a palaeoseismological trench near Postel (northeastern Belgium), as part of the programme on geological disposal of high-level/long-lived radioactive waste that is carried out by ONDRAF/NIRAS. The results of the lithological, tectonic and palaeoseismological investigations in this trench were published in Verbeeck et al. (2017), together with the initial dating results based on OSL dating and ESR dating of quartz. The dating results did not allow to bracket the depositional age of the faulted sediment more precise than roughly between ca. 1.5 Ma (OSL) and 5 Ma (ESR). The conclusion of the dating study was that the OSL results might be underestimating the true burial age, given that the natural OSL signal approaches saturation, while the ESR results would be an overestimate, given the rather poor bleaching behaviour of the ESR signals.

The objectives of this study are: (1) to extend the ESR analysis towards a better understanding of the bleaching processes involved using the multiple-center dating method and (2) to test the OSL and ESR dating results against cosmogenic ^{10}Be and ^{26}Al ages. The ultimate aim is to improve the chronostratigraphy of the faulted sediments in the trench as to precisely reconstruct their erosional history.

2 Geological and geomorphological evolution

The study area (Figure 1) is situated in the north of Belgium, near the border with the Netherlands, and in the tectonic structure known as the Campine Basin. From a geodynamic point of view, the Campine Basin is located in an intermediate position between the rapidly subsiding Roer Valley Graben in the north, and the uplifting Brabant and Ardennes Massifs in the south. The Campine Basin has witnessed a long Cenozoic burial history. Post-Rupelian marine and estuarine deposition during the last 30 Ma almost exclusively consists of (glauconite-rich) sand, up to 300 m thick (Vandenberghe et al., 2004).

The terrestrial evolution of the Campine area started with the gradual retreat of the sea during the Neogene, as a result of systematic sea level lowering and overall uplift of the bordering areas around the southern North Sea (Miller et al. 2005; Cloething et al. 2007). The Mol Formation represents a major episode in the Late Cenozoic emergence of the southern North Sea basin, as it is thought to have recorded the transition from shallow marine to fluvial facies. According to the Belgian lithostratigraphy (Laga et al., 2001), the Mol Formation is a white pure, coarse and medium to fine grained sand, sometimes lignitic and with some lenses of micaceous clay. In its type area, it is traditionally assigned to the Pliocene, more in particular the Piacenzian stage, roughly between 3.6 Ma and 2.6 Ma (Vandenberghe et al., 2004). In a western European context, the lower part of the formation is thought to be the equivalent of the Kiezelooliet Formation and the upper part would be the equivalent of the Stramproy Formation (Vernes et al., 2018; Figure 2). The latter consists of quartz-rich sands with low gravel content and originated from deposition by small river systems, the so-called ‘Belgian rivers’ (Westerhoff et al., 2003). Its chronostratigraphic position is thought to be Early Pleistocene (roughly between 2.5 Ma and 1 Ma; Westerhoff et al., 2008). Around 1 Ma at the earliest, the Rhine and Meuse shifted their course towards the west, probably as a result of tectonic movements along the westernmost Roer Valley Graben faults, including the Rauw fault (Figure 1). The Sterksel Formation (Rhine) and Zutendaal Formation (Meuse) were deposited and preserved on top of what is today known as the Campine Plateau (Figure 3). Both rivers had already shifted their course towards a more eastern position by 0.5 Ma at the latest, given the absence of Rhine deposits younger than 0.5 Ma in the depocenter of the Roer Valley Graben (Schokker et al. 2005).

During the Middle Pleistocene, the hydrography of northern Belgium drastically changed due to the 'opening' of the English Channel (Vandenberghe and De Smedt 1979). Various studies (Gibbard 2007; Gupta et al. 2007; Toucanne et al. 2009) link the opening of the English Channel to the catastrophic drainage of a large proglacial lake during marine isotope stage 12 (MIS 12), approximately 450 ka ago (Elsterian). The 450 ka event triggered the formation of a buried palaeo-channel system known as the Flemish Valley (Figure 1), with extensions towards the south and the east (Tavernier and De Moor, 1974). Undoubtedly, the area west of the Campine Plateau, including the (Kleine) Nete catchment experienced prolonged phases of erosion and denudation after the Rhine had left the region, around 0.5 Ma at the latest, and is assumed to be linked to the opening of the English Channel and the development of the Flemish Valley (Figure 1 and Figure 3; Heyse and Demoulin, 2018; Beerten et al., 2018).

Figure 1 –

Figure 2 –

Figure 3 –

3 Materials and methods

3.1 Samples

A schematic overview of the cross-section of the trench, located in the village of Postel, is shown in Figure 4. Unit A (Maatheide Member of the Mol Formation) consists of well sorted, well rounded, and medium to coarse quartz sand. The lowest subunit A1 is white sand with vague horizontal layering, recognisable by thin discontinuous grey bands. The second subunit A2 is a 0.5 to 1 m thick layer of black detrital organic-rich sand and some fine, discontinuous clay lenses. Horizontal layering with different amounts of organic material, fine ripple marks and bioturbation indicate that this is a depositional unit and not post-depositional illuviated organic material. Subunit A3 consists of the same kind of quartz sand as subunits A1 and A2, but stands out because of its (chocolate) brown colour, which is due to coatings of organic material around the grains. The unit shows faint indications of large foresets, dipping slightly to the northeast. Subunit A4 also consists of brown sand, but with increasingly steep north-eastward dipping and downlapping large-scale foresets, with an angular block of peat at the base. Unit A is interpreted as a fluvio-estuarine deposit. This interpretation is based on the relatively coarse grain size, and the occurrence of large-scale foresets which presumably represent a prograding bedform. Its grain-size is fairly continuous throughout the trench, with the median situated around 350 µm, and >80% of the grains in the range between 250-500 µm (Verbeeck et al., 2017). Indicators for a full estuarine environment, such as clay drapes, are lacking, as well as indicators for aeolian influence. However, given these observations, and taking into account the overall geological evolution of the area during the Neogene and Quaternary (see section 2), the sediments of unit A have been deposited at the transition from a fluvial to an estuarine environment. The gravelly Sterksel Formation (fluvial sands from the Rhine) is not present in the trench, only some pebble and cobble-sized ventifacts (i.e., wind-abraded rock fragments) remained following complete erosion of this deposit. The pebble and cobble layer is covered by several thin layers of Late Quaternary deposits, aeolian or fluvio-aeolian in origin, that are deformed by cryoturbation, but not displaced by the fault (units B to F).

Two sampling positions were targeted for ESR, OSL and CRN dating (Table 1; Table 4). Sample GLL-153104 (abbreviated as sample -04 throughout the text) originates from unit A1 and was taken from the footwall, at a depth of 248 cm below the surface (i.e., at an altitude of 34.7 m T.A.W.). Sample GLL-153103 (abbreviated as sample -03 throughout the text) originates from the younger unit A4 and was taken from sediment in the hanging wall, at a depth of 164 cm below the surface (i.e., at an altitude of 33.7 m T.A.W.). A first set of subsamples was taken by hammering 12 cm wide and 20 cm long PVC tubes in the freshly scraped wall. The tubes were then lidded, duct taped and wrapped in thin foil. This first set of subsamples was used to determine the OSL and ESR dose, as well as the dose rate since they contained enough surrounding material. A second subset consisted of bulk material laterally collected from the remaining holes in the wall, each around 1.5 kg, and was used for CRN dating.

Since all three dating methods rely in various degrees on the burial history of the sample, a detailed assessment of the overburden thickness variation through time is included. It can clearly be seen from Figure 3 that the present-day sample depth below the surface is not representative for the average depth during the time of burial. Laloy et al. (2017) determined that an amount of ca. 10 m sediment would have been eroded from the top of the Campine Plateau, which means that the amount of eroded material at the trench site is even more, given its lower topographical position. Subtracting the current sample elevation from the inferred palaeo-surface elevation prior to erosion leads to a maximum burial depth of ca. 22 m and 24 m for samples GLL-153103 and GLL-153104 respectively (Figure 3). This maximum burial depth would have been achieved around 0.5 Ma at the latest (Laloy et al., 2017; Beerten et al., 2018; see also section 2) after sediment had been deposited in two major phases, one prior to 1 Ma, and another one between 0.5 Ma and 1 Ma.

Figure 4 –

Table 1 –

3.2 Trapped charge dating

3.2.1 Principle of burial dating using ESR and OSL

3.2.1.1 ESR dating of sedimentary quartz

The physical basis of ESR spectroscopy is explained in, e.g., Grün (1989). ESR spectroscopy is used to detect paramagnetic centers, such as trapped electrons and/or holes in geological materials. The principle of ESR spectroscopy is based on the absorption of microwave energy at such defect sites in, e.g., quartz, while being embedded in a magnetic field. The atomic environment and the specific characteristics of the defect site determine the magnitude of the magnetic field at which microwaves are absorbed. The relative defect concentration is directly proportional to the microwave absorption, and the recorded ESR signal.

Crystalline quartz, i.e. the chemical entity SiO_2, is one of the most abundant minerals in sediments. Several paramagnetic defects in quartz are known to be useful for geological dating using the ESR technique. Such centers, i.e., trapped charge, are formed due to ionising radiation (alpha, beta and gamma-rays) from surrounding radioisotopes of U, Th and K, and cosmic rays. As such, the relative defect concentration in a quartz sample is a measure for the totally accumulated radiation dose, also called the equivalent dose (D_e), which is expressed in gray or kilogray (Gy or kGy). If also the dose rate (D, expressed in Gy/ka or kGy/ka), in the immediate environment of the sample is known, the time t (expressed in ka or Ma) elapsed since the last zeroing event can be calculated according to

$$t = \frac{D_e}{D} \qquad \text{(Eq. 1)}$$

In order for the method to be reliable, any pre-existing ESR signals should be erased prior to the event to be dated. The zeroing process responsible for resetting the geological clock is dependent on the geological context of the quartz mineral. Several ESR centres (such as Ti- and Al-centres) have proven to be light-sensitive, and offer the opportunity to determine the moment of the last exposure to sunlight, prior to burial. The accuracy of the ESR age is dependent on the completeness of this zeroing process. Incomplete signal zeroing inevitably will lead to age overestimates. Conversely, unstable signals may lead to age underestimates. Therefore, the mean lifetime of ESR centres should be large enough to cover the geological period of interest.

3.2.1.2 OSL dating of sedimentary quartz

Optically stimulated luminescence (OSL) dating of unburnt sediments works on the same principle as ESR dating in that it is based on the time-dependent accumulation of radiation damage in minerals. Exposure to sunlight is the resetting agent, and the clock starts ticking anew once shielded from sunlight. OSL differs from ESR in the way the radiation damage is detected; it is detected as a small amount of light ("luminescence") that is emitted when the mineral grains are exposed to light with a longer wavelength.

The most widely used dating procedure at present uses the fast component of the quartz OSL signal and the single-aliquot regenerative-dose (SAR) procedure for D_e determination. This approach is considered as a reliable chronological tool in a range of geomorphological settings (see e.g. Murray and Olley, 2002; Wintle and Murray, 2006; Wintle, 2008, and references therein; Madsen and Murray, 2009; Rhodes 2011). It is also the approach applied in this work (see further). Apart from D_e determination, determination of the dose rate and calculation of the age (see Eq. 1) is the same as for ESR dating.

3.2.2 Sample preparation

Sample preparation for OSL and ESR dating was done in the Ghent Luminescence Laboratory (Ghent University). From the inner material of the sampling tubes quartz grains (125-180 µm) were extracted using conventional sample preparation procedures (HCl, H_2O_2, sieving, density separation and etching for 60 mins with 40% HF). The purity of the quartz extracts was confirmed by the absence of a significant infrared stimulated luminescence (IRSL) response at 60 °C to a regenerative β-dose. The sensitivity to infrared stimulation was considered to be significant if the resulting IRSL signal amounted to more than 10% of the corresponding OSL signal (Vandenberghe, 2004) or if the OSL IR depletion ratio deviated by more than 10% from unity (Duller, 2003). For dose rate determination, the surrounding sediment was dried at 110 °C (until constant weight), homogenized and pulverized. A subsample of about 130 g was then cast in wax (see e.g. De Corte et al., 2006) and stored for one month before being measured.

3.2.3 Dose determination

3.2.3.1 ESR dating

The etched quartz grains were divided into several aliquots (~ 300 mg) for ESR measurements. Individual aliquots were irradiated with Co-60 gamma rays in the BRIGITTE irradiation facility of SCK•CEN (BR2 reactor) at a dose rate of 3.22 (±2%) kGy/h, resulting in the following dose sequence (kGy): 0.44-0.89-1.79-3.57-5.36-7.14-10.71-14.29-19.64. The dose rate was calibrated with red perspex and corrected for the different absorption coefficient relative to quartz (Berghmans, 2001).

Individual aliquots were measured at cryogenic temperatures (ca. 100 K) in a Bruker X-band ESR spectrometer operating at a microwave frequency of ~ 9.2 GHz (Geographisches Institut der Universität zu Köln). Each aliquot was measured once, assuming that angular dependence is negligible using 300 mg of quartz.

The multiple-aliquot additive-dose (MAAD) multiple-center method was applied using Ti- and Al-impurity centres in quartz (Toyoda et al., 2000; Duval et al., 2015). Measurement settings were selected according to procedures described in Beerten et al. (2008) and different absorption lines were used for dose determination. Error ranges represent the standard error of the fitting procedure. The signal intensity of Ti-impurity centres was determined using ESR absorption line 1 from Beerten et al. (2008) for Ti-Li centres, and absorption line 2 for a mix of Ti-Li and Ti-H centres. The relatively low signal-to-noise ratio did not allow to measure Ti-H centres individually. The signal intensity of Al-impurity centres was determined according to procedures described in Voinchet et al. (2007). Subsequently, the equivalent dose was calculated using the thus constructed dose curves (including the natural, unirradiated, aliquot). Equivalent doses were estimated through extrapolation of the dose response curve using a single saturating exponential and a double saturating exponential function with opposite sign for the Ti-impurity centres (Duval and Guilarte, 2015). A double saturating exponential with equal (positive) sign (Voinchet et al., 2015) and a single saturating exponential plus linear function (Duval, 2012) was used for the Al-impurity centres.

The obtained equivalent dose was corrected for the unbleachable residual (Al centres), according to procedures described in Voinchet et al. (2015). Aliquots were bleached for 10h, 100h and 1000h using a SOL-2 sunlight simulator (Hönle). Error weighting was not applied since only one measurement per aliquot was done.

3.2.3.2 OSL dating

All analyses were carried out on grains spread on the inner 8 mm of 9.7 mm stainless steel discs. The luminescence measurements were made with a Risø TL/OSL-DA-15 reader, equipped with high power blue diodes emitting at 470 ± 30 nm and IR diodes emitting at 875 nm (Ghent Luminescence Laboratory, Ghent University). All luminescence emissions were detected through a 7.5 mm thick Hoya U-340 UV filter. Irradiations were carried out with a 90Sr/90Y β-source mounted on the reader. Details on the measurement apparatus can be found in Bøtter-Jensen et al. (2003) and references therein. The equivalent dose (D_e) was determined using the single-aliquot regenerative-dose (SAR) protocol as described by Murray and Wintle (2000; 2003). Optical stimulation with the diodes was for 38.5 s at 125°C. The initial 0.31 s of the decay curve, minus a background evaluated from the 0.31 – 1.08 s interval, was used in the calculations. For both samples, the dependence of D_e on preheat temperature (10 s) was investigated. A dose recovery test was performed to assess the suitability of the SAR laboratory measurement procedure. For each sample, six natural aliquots were first bleached using the blue diodes at room temperature (2 times 240.5 s, separated by a 10000 s pause); they were then given a dose equal to the estimated D_e and measured using the SAR protocol employing a preheat of 10 s at 240°C. In all experiments, measurements of the test-dose signal were preceded by a cut-heat to 160°C, and followed by a stimulation with the blue diodes for 38.5 s at 280°C.

3.2.4 Dose rate determination

Low-level high-resolution gamma-ray spectrometry was used for the determination of the natural dose rate (see Hossain, 2003 and Vandenberghe, 2004 for details). The annual dose was calculated from the present-day radionuclide activities using the conversion factors of Adamiec and Aitken (1998). A factor of 0.9 (± 5% relative uncertainty) was adopted to correct the external beta dose rates for the effects of attenuation and etching, following Aitken (1985; Appendix C; and references therein). We assumed that etching made the external alpha contribution negligible. An internal dose rate of 0.013 Gy/ka was assumed (Vandenberghe et al., 2008). The same conversion and correction factors, and the same internal dose rate were thus used as the ones in Verbeeck et al. (2017). A reassessment of conversion factors was made by Guérin et al. (2011) and an update of correction factors can be found in Brennan (2003). As the region has experienced significant geomorphological changes since deposition of the sand samples, a detailed assessment of the water content and burial depth variations seemed necessary. Both the beta and gamma contributions were corrected for the effect of moisture as outlined by Aitken (1985). The low radionuclide concentrations in quartz-rich samples may cause the cosmic rays to contribute significantly to the total dose rate. The contribution of cosmic radiation was iteratively calculated following Prescott and Hutton (1994), time-averaged using the inferred burial history and assuming a maximum burial depth of 22 m and 24 m for samples GLL-153103 and -04 respectively. The saturated gravimetric water content was estimated to be 0.24 ± 0.01 g/g. The burial history was subsequently translated into water content history, assuming the saturation at initial deposition was 90% since these are shallow fluvial sands. From the saturation history we calculated the time averaged water saturation of the sample to 95 ± 6 % and 96 ± 4 % for samples GLL-153103 and -04, respectively.

3.3 Cosmogenic radionuclide dating

3.3.1 Principle of CRN burial dating and surface dating

The principle of simple burial dating using CRNs is based on the assumption of instantaneous and complete burial of the sediment following deposition, without significant erosion (i.e., complete shielding from secondary cosmic ray production). The concentration ratios of two CRNs with different half-lives will only depend on these half-lives if there is no significant post-burial production. The age equation can be written as (Balco and Rovey, 2008):

$$t_{\mathrm{B}} = \frac{-\ln(R_M/R_{init})}{(\lambda_{26}-\lambda_{10})} \qquad \text{(Eq. 2)}$$

where t_B [a] is the total burial age since the time of deposition, R_M [-] is the measured $^{26}Al/^{10}Be$ ratio in the sample, R_{init} [-] is the spallogenic $^{26}Al/^{10}Be$ production ratio at the surface (at the time of deposition), λ_{26} [a^{-1}] is the decay constant of ^{26}Al and λ_{10} [a^{-1}] is the decay constant of ^{10}Be. If the assumption of instantaneous and complete burial has not been met, the resulting ages will always underestimate the true burial age. To apply this simple burial dating technique, the $^{26}Al/^{10}Be$ ratio of at least one sample is required (Gosse and Klein, 2015).

To check the validity of equation (2) and its underlying assumptions, we used the cosmogenic radionuclide profiling equations (see, e.g., Braucher et al., 2009, and Hidy et al., 2010) to determine the age of the samples. As any erosion event might have been preceded by an episode of deep burial, the unknown age *t* was split up into two components. The first one is associated with the time period during which CRNs were accumulating under zero-erosion and deep burial conditions, while the second one corresponds to the time period during which CRNs were accumulating under steady-state erosion conditions. The accumulation of CRNs, $N_{total}(z,t)$ [atoms/g], in a sample thus can be described by a mathematical function composed of three terms that represent (1) the inherited CRN concentration of the sediment, N_{inh} [atoms/g], (2) the post-depositional production of CRNs after burial but prior to erosion, $N_{left}(z)$, and (3) the post-depositional production of CRNs during the erosional event, $N_{erosion}(z)$:

$$N_{total}(z,t) = N_{inh} + N_{erosion} + N_{left} \qquad \text{(Eq. 3)}$$

with

$$N_{left} = \left(\sum_i P_i(0) e^{-\frac{z_0\rho}{\Lambda_i}}(t_B - t_E)\right)e^{-\lambda t_B} \qquad \text{(Eq. 4)}$$

where

t_B being the total burial time of the sample since deposition, and t_E the time since the start of erosion,

and

$$N_{erosion} = \sum_i \frac{P_i(0)}{\lambda+\frac{\rho E}{\Lambda_i}} e^{-\left(\frac{\rho(z_0-Et_E)}{\Lambda_i}\right)}\left(1-e^{-\left(\lambda+\frac{\rho E}{\Lambda_i}\right)t_E}\right) \qquad \text{(Eq. 5)}$$

where

E is the post-depositional erosion rate in cm/a (m/Ma × 10^{-4}), t_E [a] is the exposure age (which equals here the time since the start of erosion), λ [1/a] is the decay constant ($\lambda = \ln 2 / t_{1/2}$), z_0 [cm] is the initial shielding depth prior to erosion ($z = z_0 - Et_E$), ρ [g/cm³] is the density of the overlying material, and Λ_i [g/cm²] is the attenuation length. The CRN production rate, $P_i(z)$ [atoms/g/a], is a function of the depth, z [cm], below the surface as:

$$P_i(z) = P_i(0)e^{-\frac{z\rho}{\Lambda_i}} \qquad \text{(Eq. 6)}$$

The subscript '*i*' indicates the different production pathways of in-situ produced ^{10}Be and ^{26}Al via spallation, muon capture and fast muons, following Dunai (2010). In this study, the relative spallogenic and muogenic production rates are based on the empirical muogenic to spallogenic production ratios established by Braucher et al. (2011). The effective attenuation length for the sampling position was obtained using Table 4 in Marrero et al. (2016), and equals 152 g/cm². For fast and stopped muons, the attenuation length was set at respectively 1500 and 4320 g/cm² following Braucher et al. (2011). Production rates were scaled following Stone (2000) with a sea level high latitude production rate of (4.49 ± 0.30) atoms/g/a for ^{10}Be, and a total $^{26}Al/^{10}Be$ production ratio of 6.75. The bulk density, ρ, of the sediment was set to 1.7 g/cm^3, which is consistent with the average value of upper Neogene and Quaternary sediments in the region (Beerten et al., 2010). A half-life of

1.387×10^6 years was used for ^{10}Be (Chmeleff et al., 2010) and 7.17×10^5 years for ^{26}Al (Norris et al., 1983). Given the flat topography of the Campine Plateau, topographic shielding was negligible and therefore not corrected for (Norton and Vanacker, 2009).

3.3.2 Sample preparation

Samples were prepared at the UCLouvain Cosmogenic Isotope Laboratory (Louvain-la-Neuve). *In situ* produced ^{10}Be and ^{26}Al was extracted from purified quartz using standard separation methods described in von Blanckenburg et al. (1996) and Vanacker et al. (2007). Two blanks were processed. Approximately 200 µg of ^{9}Be carrier was added to blanks and samples containing 30 to 35 g pure quartz. The purified quartz was subsequently dissolved in concentrated HF, from which beryllium and aluminium is stepwise extracted using anion/cation exchange column chemistry. Remaining precipitates were oxidized and pressed into copper targets. Finally, ^{10}Be/^{9}Be and ^{26}Al/^{27}Al ratios were quantified using the 500 kV Tandy facility at ETH Zürich (Christl et al., 2013). The ^{10}Be/^{9}Be ratios were normalized with the in-house standard S2007N and corrected with a blank ^{10}Be/^{9}Be ratio of $(4.06 \pm 0.23) \times 10^{-15}$. The ^{26}Al/^{27}Al ratios were normalized to the ETHZ in house standard ZAL02 with a nominal ^{26}Al/^{27}Al ratio of $(46.4 +/- 0.1) \times 10^{-12}$ and corrected with a blank ^{26}Al/^{27}Al ratio of $(7.1 \pm 1.7) \times 10^{-15}$ following Lachner et al. (2014). Total Al concentrations of the samples were determined by inductively coupled plasma optical emission spectrometry (ICP-OES) at the Earth and Life Institute of the University of Louvain. The analytical uncertainties on the isotope ratios of sample and blank are then propagated into the 1σ analytical uncertainty for nuclide concentrations. This includes the uncertainty on the ICP-OES measurements for Al.

3.3.3 Bayesian inference

The following 8 parameters were jointly estimated by inversion of the measured ^{10}Be and ^{26}Al concentrations and their ratios in the two samples: the z_0 values for GLL-153103 and -04 (z_{01} and z_{02} respectively), the total burial time (t_{B1} and t_{B2}), the time elapsed since the beginning of the erosional event (t_{E1} and t_{E2}) and the inherited ^{10}Be and ^{26}Al concentrations of the sediment ($N_{inh}{}^{10}Be$ and $N_{inh}{}^{26}Al$).

We apply an overall similar Bayesian inversion approach as in Laloy et al. (2017) to infer the posterior distribution of $\mathbf{x} = \left[z_{01}, z_{02}, t_{B1}, t_{B2}, t_{E1}, t_{E2}, N_{inh}{}^{10}Be, N_{inh}{}^{26}Al\right]$. In the Appendix we describe the differences between the approach developed herein and that proposed by Laloy et al. (2017).

Based on the current geomorphological knowledge of the region (Beerten et al., 2018; Laloy et al., 2017), the initial shielding depth (prior to the start of erosion) was set to a uniform prior distribution between 6 m and 36 m for sample GLL-153103 and between 8 m and 38 m for sample GLL-153104. The inherited concentration is assigned a uniform prior, equal for both samples, ranging between 0-50000 atoms/g for ^{10}Be and 0-200000 for ^{26}Al, which comprises the full range between zero and the actually measured radionuclide concentration. The minimum and maximum OSL and ESR ages were used to set the uniform prior bounds for t_{B1} and t_{B2} (see Table 2 and Table 3), while the prior distributions for t_E were set to uniform distributions between 0 Ma and 4 Ma. The latter allows for a wide range of values to be picked up by the algorithm. Furthermore, the following boundary conditions were implemented in the code: $t_E < t_B$ (since the latter represents the total burial time) and E < 70 m/Ma (given the very low likelihood of higher values for outcrop erosion rates in Portenga and Bierman (2011)).

4 Results

4.1 Trapped charge dating

4.1.1 Dose rate determination

The individual activities of radionuclides ^{40}K, ^{234}Th, ^{226}Ra, ^{210}Pb and ^{232}Th are shown in Table 2. The high quartz content of the sediment is clearly reflected in the very low activities for radioisotopes of U, Th and K. Total dose rates are very low, around 0.16-0.19 Gy/ka. It has to be noted that the cosmic dose rate, iteratively derived from the burial history, contributes for more than 25% to the total dose rate. A detailed discussion on the burial history is given in section 5.1. Furthermore, the internal alpha contribution is around 5-10% of the total dose rate. There are no indications of secular disequilibrium in the U-series, within the given uncertainty limits.

Table 2 –

4.1.2 ESR dating

The bleaching behaviour of relevant ESR centres in the two samples is shown in Figure 5. Both samples show different bleaching characteristics. For sample -03, Ti centres are initially bleaching at a higher rate than Ti-Li centres, while both are completely zeroed after 100 hours bleaching time. In contrast, the Al centre is not fully bleached yet even after 1000 hours (see, e.g., Voinchet et al., 2003). It appears that the residual signal is relatively small, down to ca. 10% of the initial Al intensity. For sample 3104, Ti and Ti-Li centres are completely zeroed after 10 hours bleaching time, while Al centres remain at ca. 60% of the initial signal intensity after 1000 hours. Even though it cannot be assured that the Al signal has reached a stable signal intensity after 1000 hours bleaching time, this residual (after 1000 hours) is used to correct for the unbleachable residual.

Figure 5 –

Dose response curves for Ti and Al centres are shown in Figure 6. It can be observed that the Ti-signal shows a decreasing trend with doses above 10 kGy (Figure 6a and b). Such behaviour of the Ti-signal has previously been reported by Woda and Wagner (2007) and Duval and Guilarte (2015). The same observation, though somewhat less clearly expressed, can be made for Ti-Li centres in sample -04 (Figure 6d). This may suggest that mainly H-compensated Ti centres are responsible for this particular dose behaviour. Given the sensitivity of calculated equivalent doses on the fitting equation used (Duval and Guilarte, 2015), two different approaches were adopted to calculate the Ti-related equivalent doses: a double saturating exponential with opposite sign, and a single saturating exponential. As can be seen in Table 3, there is no significant difference between the individual methods if applied on the same ESR centre. In the case of the Al-related centres, two different functions were fitted to the dose points: a double saturating exponential with equal (positive) sign, and a single saturating exponential plus linear function (Figure 6e and f). Again, there is no significant difference between both fitting methods if applied on the same ESR centre (Table 3).

Figure 6 –

The corresponding ESR ages are shown in Table 3. There seems to be a large in-sample variation, and none of the ages converge to a single solution for one of the samples. As can be seen, the Ti-Li and Al-based ages do more or less coincide for sample -03, but the Ti-based age is much younger. On the contrary, for sample -04 it seems that the Ti-Li and Ti-based ages coincide, while the Al-based age is much older. The younger Ti-based age for sample 3103, in comparison with the Ti-Li and Al-based age, can be explained by the faster bleaching rate of Ti centres in that sample (Figure 5). The older Al-based age for sample -04 can only be explained by incomplete bleaching. The apparent age inversion (the upper sample apparently being older than the lower sample, i.e., ca. 12 Ma vs. ca. 5 Ma) based on Ti-Li centres is very likely due to the faster bleaching rate of these centres in the oldest sample (complete bleaching after 10 hours) in comparison with the youngest sample (complete bleaching after 100 hours). There thus seem to be clear indications of incomplete bleaching of the Al centre in both samples, even after correcting for the unbleachable residual. . The youngest ages, (based on Ti centres) should be regarded as better estimates of the true burial age, even for the oldest sample (-04). As such, ESR ages of 4.8 ± 1.8 Ma and 4.5 ± 2.2 Ma are taken forward in the discussion for the oldest and youngest sample respectively.. They are based on fitting a single saturating exponential curve to the dose points, and are in agreement, within 1σ errors, with age estimates based on the double exponential curve fitting with opposite sign (see Table 3).

Table 3 –

4.1.3 OSL dating

The effect of the preheat on measurements of natural doses (D_e) is shown in Figure 7. While no systematic dependence in D_e with preheat temperatures up to 280°C can be observed, the correction for sensitivity changes occurring throughout the SAR sequence becomes progressively more inaccurate from temperatures of 260°C onwards. In the 260 – 300°C temperature range, the recycling ratio systematically decreases for sample GLL-153103, while the opposite trend is observed for sample GLL-153104. For these two samples, the average D_e (± 1 standard error) across the 160 – 240°C temperature region was used in the final age calculations (Table 3). The D_e values thus obtained are in the range of 250 – 260 Gy. The corresponding OSL ages are 1.4 ± 0.2 Ma and 1.6 ± 0.2 Ma for sample -03 and -04 respectively. Interestingly, while the natural OSL signal intersects with the high-dose, non-linear region of the laboratory dose-response curve, it lies below its saturation level (Figure 8). The dose recovery test yielded an overall average measured to given dose ratio (± 1 standard error) of 0.89 ± 0.03 (n = 12); the corresponding values for the recycling ratio and recuperation (expressed as % of the sensitivity-corrected natural OSL signal) are 1.000 ± 0.004 and 0.06 ± 0.01%, respectively. It implies that a known laboratory dose of the order of about 250 Gy, administered following optical resetting but prior to any heating treatment, can be measured to within 10%.

Figure 7 –

Figure 8 –

4.2 Cosmogenic radionuclide dating

4.2.1 Simple burial dating

Analytical results are shown in Table 4. Overall, the cosmogenic radionuclide concentrations are small, and associated errors relatively large, i.e., within one order of magnitude of the measured value. The Al and Be concentrations for sample GLL-153103 are $(2.28 \pm 0.75)\times 10^5$ at/g and $(5.31 \pm 0.60) \times 10^4$ at/g respectively, while those for sample GLL-153104 are $(1.85 \pm 0.64) \times 10^5$ at/g and $(4.96 \pm 0.39) \times 10^4$ at/g respectively. The corresponding $^{26}Al/^{10}Be$ ratios allow to calculate a minimum burial age for both samples, given the fact that the condition of instantaneous and complete burial has not been met. The thus obtained minimum burial ages are 0.9 ± 0.7 Ma for sample GLL-153103 and 1.2 ± 0.8 Ma for sample GLL-153104 (Table 5). Note the large uncertainties associated with these results. They are due to the relatively large errors on the individual nuclide concentrations, especially that of ^{26}Al.

Table 4 –

Table 5 –

4.2.2 Surface exposure dating

The marginal posterior distributions as obtained by Bayesian inversion of the Al-Be data are shown in Figure 9. The posteriors for the total burial age since the time of deposition, t_B, and the initial shielding depth prior to erosion, z_0, show a wide distribution with probability densities ranging up to a factor of two (Figure 9a-d). These distributions do not show a significant tendency and are poorly resolved. In contrast, the posteriors for the time since the start of erosion, t_{E1} and t_{E2}, are slightly better resolved than their uniform prior (Figure 9g-h). The central 68% of the distributions is comprised between 0.6-2.6 Ma for t_{E1} and 0.7-3.1 Ma for t_{E2}. The median value and associated median absolute deviation of these distributions is 1.4 ± 0.7 Ma and 1.7 ± 0.9 Ma for t_{E1} and t_{E2} respectively (Table 6). The posterior distributions for the inherited ^{10}Be and ^{26}Al concentrations are widely spread though the ^{26}Al distribution is skewed towards zero. However, if corresponding t_E-z_0 pairs are combined to produce an estimate for erosion rate (E), the resulting distributions are relatively sharp, though skewed, with a median value (and associated median absolute deviation) of 15 ± 8 m/Ma for E_1 (sample GLL-153103) and 13 ± 9 m/Ma for E_2 (sample GLL-153104).

Table 6 –

Figure 9 –

5 Discussion

5.1 Integration of the dating results

The results from the ESR, OSL and CRN techiques are shown together for comparison in Table 7. The ESR ages are based on Ti centres (absorption line 2 in Beerten et al., 2008), because these systematically show younger ages compared to Ti-Li and Al centres. The Ti-H centre is also known to be a suitable ESR centre to detect relatively small doses, in the range of several 100 Gy (Bartz et al., this volume). However, the corresponding ESR signal could not be properly quantified in the present study, because of the very weak or sometimes even absent signal. As such, the Ti-based ESR ages suggest that the Mol Formation was deposited around 4.5-4.8 Ma. However, the uncertainties associated with these ages are relatively large, roughly between 30% and 50% (1σ). The ESR age of the oldest sample suggests that it was deposited between 3.0 Ma and 6.6 Ma, with a probability of ca. 68%, and between 1.2 Ma and 8.4 Ma, with a probability of 95%. For the upper sample, the intervals are between 2.3 Ma and 6.7 Ma, and between 0.1 Ma and 8.9 Ma. Thus, depending on the chosen confidence level, these ages are either in or not in agreement with the anticipated stratigraphical age of 2.6 Ma to 3.6 Ma (Vandenberghe et al., 2004).

The large ESR age uncertainty reflect the scattered appearance of individual dose points in the dose response curves. This is attested by the fact that the ESR ages with the largest errors are associated with the smallest coefficients of determination in the fitting procedure. The scatter may be due to the fact that only one single measurement per aliquot was done, without verifying the angular dependence of the ESR signals. Furthermore, dose estimates from time delayed repeated measurements may lead to equivalent dose discrepancies of up to 25% (Kreutzer et al., 2018). Another factor that may introduce supplementary errors is the fact that the first dose step is quite large with respect to the measured dose (Kreutzer et al., 2018). It is ca. 50% of the smallest ESR doses measured, and even 200% if we accept the OSL dose as a better estimate of the true burial dose. Indeed, given the rather slow bleaching behaviour of ESR centres compared to the OSL fast component incomplete bleaching cannot be ruled out for the studied samples, as they are deposited in a fluvial-estuarine environment. This may well explain the ESR age overestimate relative to the OSL age.

Trapped charge dating of low dose rate samples is challenging for two reasons. First of all, the burial history becomes crucial since it has a large impact on the time averaged cosmic dose rate. The latter contributes for more than 25% to the total dose rate for the studied samples. In addition, the impact of incomplete bleaching on the measured dose becomes larger with decreasing dose rates. For relatively slowly bleaching trapped charge such as observed by ESR spectroscopy, this may lead to significant age overestimates.

Table 7 –

Figure 10 –

The OSL equivalent doses are significantly lower than the ESR doses (they differ by ca. 800 Gy and 500 Gy for sample -03 and -04 respectively), which leads to significantly lower OSL ages, clustering around 1.5 Ma. The quartz extracts exhibit satisfactory luminescence characteristics in terms of brightness (clearly distinguishable from the background) and OSL decay (dominated by the fast component). The SAR measurement procedure appears suitable for application to the samples as indicated by negligible signal recuperation and recycling ratios consistent with unity. It is possible to recover a known laboratory dose to within 10%, and D_e values show a plateau across a range of preheat temperatures. Even though the OSL doses are much lower than the ESR doses, they are quite high (ca. 250 Gy); their natural signal intersects with the non-linear region of the laboratory dose-response curve, but below its saturation level. These growth curves can be represented well by the sum of two saturating exponential functions. It remains to be established whether reliable D_e values can be obtained in such high dose regions, especially when the dose response cannot be described by a single saturating exponential function (see e.g. Timar-Gabor et al., 2012; Timar-Gabor and Wintle, 2013).

The simple burial CRN ages (Table 5), are 0.9 ± 0.7 Ma for sample -03 and 1.2 ± 0.8 Ma for sample -04. The relative standard deviation is quite large, which is due to the fairly low cosmogenic radionuclide concentrations and the analytical uncertainty on the $^{26}Al/^{27}Al$ ratio. The geomorphological setting suggests that the assumption of simple burial and complete shielding is not valid, given the relatively shallow sampling depth. Indeed, geomorphological reconstructions (Laloy et al., 2017; Beerten et al., 2018) suggest that the sampling area was subject to erosion, in which case there must have been at least some post-depositional cosmogenic radionuclide build-up. In that case, the simple burial dating technique as applied here only yields aminimum age. The Bayesian inversion of the Al-Be data allows to constrain the onset of erosion, and the erosion rate. We refer to the former as the CRN surface ages, as they represent the time after which the sediments have been exhumed and moved closer to the surface as a result of erosion. The median CRN surface ages, which explicitly take into account post-depositional radionuclide build-up, are logically larger than the CRN burial ages, i.e. 1.4 ± 0.7 Ma for sample -03 and 1.7 ± 0.9 Ma for sample -04. Though the OSL and CRN surface ages are seemingly consistent, they reflect different geomorphological processes. The OSL age, if correct, is the burial age of the sediment, while the CRN surface age is the onset of subsequent exhumation of the previously buried sediments. In summary, the OSL and ESR data indicate that unit A has been deposited prior to ca. 1.4 ± 0.2 Ma (the OSL age of the youngest sample), but probably not earlier than ca. 4.8 ± 1.8 Ma (the ESR age of the oldest sample). In addition, the CRN exposure ages of 1.4 ± 0.7 Ma and 1.7 ± 0.9 Ma suggest that erosion started sometime during the Early Pleistocene.

5.2 Implications for the local and regional geological and geomorphological history

The burial age of unit A cannot be resolved better than the time window between ca. 1.5 Ma and ca. 5 Ma, based on OSL and ESR dating. These findings do not contradict with the sequence stratigraphical age of ca. 3.6-2.6 Ma for the Mol Formation (Vandenberghe et al., 2004). However, our results suggest that an Early Pleistocene age for the studied sediment cannot be excluded. In any case, the CRN surface ages suggest that the surface which developed after deposition of the studied samples, started to erode around between 2.6-3.1 Ma at the earliest and 0.6-0.7 Ma at the latest (see Table 5).

By far the most relevant implication can be drawn from the post-depositional erosion rate of ca. 15 m/Ma. Even though the spread on this estimate is relatively large (up to 50%), it is significantly smaller than the erosion rate estimate for the Lommel Sands in the MHR quarry, a few km to the east of the present study site (see Figure 3). Laloy et al. (2017) calculated an average erosion rate of 39 ± 8 m/Ma for that site. This difference is not only surprising because of the proximity of both study sites, one would also expect the erosion rate to be larger for the Postel trench site given the fact that a larger sediment column has been removed by erosion. The difference in erosion rate between both sites can thus only be explained by considering the time window over which the erosion rate has been integrated (Figure 10).

For the MHR site, the erosion rate estimate is valid for erosion of the Lommel Sands, estimated to have been deposited between ca. 0.5-1 Ma. Based on the current dating results the sediments of unit A are at least 1 Ma older than the Lommel Sands, and probably even older (Vandenberghe et al., 2004; Figure 10a). For instance, the Postel site may have already experienced erosion from 1.5 Ma onwards, and most likely even earlier (Figure 10b-c), witnessing a total of 25 m post-depositional erosion, while the MHR site witnessed another sedimentation phase prior to 0.5 Ma (Figure 10d), and then experienced ca. 15 m post-depositional erosion (Figure 10e). In addition, the erosion rate for both samples from the Postel trench (GLL-153103 and GLL-153104) is almost, if not completely, identical. This is somewhat surprising since an initial offset of ca. 6-7 m is evident prior to normal faulting of the Rauw fault. Erosion rate E_1, corresponding to sample GLL-153103, should be significantly smaller than E_2 (corresponding to sample GLL-153104), unless fault activity mainly took place prior to the major phase of erosion (Figure 10c). In summary, the main features of this revised burial-erosion history are: (1) a sediment column developed at the site, probably well into the Early-Pleistocene, with a palaeo-surface above the present-day surface (several decameters; Figure 10a-b); (2) the last major phase of normal faulting preceded the onset of increased erosion (Figure 10c); (3) the erosion rate integrated over the last ca. 1-2.5 Ma is smaller than that integrated over the last 0.5-1 Ma (Figure 10b-e). Increasing erosion and/or denudation during the course of the Middle Pleistocene may be related to enhanced uplift of the Ardennes and the wider region north of it (van Balen et al., 2000; Rixhon and Demoulin, 2018), and/or sudden base level lowering as a result of the opening of the English Channel ca. 0.5 Ma ago (Gupta et al., 2017). Since the smallest erosion rate is observed for the finer sediment (unit A at Postel), the variations cannot be explained by lithology.

6 Conclusion

The application of the multiple-centre ESR dating method on quartz grains from two samples taken in the Mol Formation in northeastern Belgium (Campine) strongly suggests that a significant proportion of grains were incompletely or insufficiently bleached prior to burial. The best estimate ESR age of ca. 5 Ma should be regarded as an absolute upper age limit for the studied samples. The quartz OSL ages of ca. 1.5 Ma serve as a best estimate for the lower age limit. Bayesian inversion of the Al-Be data suggests that the palaeo-surface started eroding around 1 Ma at the latest. The integrated erosion rate over this approximate age window is ca. 15 m/Ma. This estimate is smaller than the one obtained in a previous study for a site ca. 5 km to the east, but can be explained in terms of the integration time window. The erosion rate observed at that site is up to 2.5 times larger but applies to younger sediment and a smaller time window. Erosion in the region accelerated sometime around 0.5 Ma, roughly speaking during the Middle Pleistocene, but the timing of this change cannot be determined more accurately. Most likely normal faulting along the Rauw fault already ceased prior to the phase of accelerated erosion in this particular area. For future work, we suggest to apply a denser CRN sampling scheme in the form of a vertical profile (depth profiling technique) to confirm the anticipated burial and surface exposure ages, and to confirm the increasing erosion rate over time.

7 Appendix

Our Bayesian inversion approach relies on Markov chain Monte Carlo (MCMC) sampling to derive the posterior probability density function (pdf) of the parameters $\mathbf{x}$

$$p(\mathbf{x}|\mathbf{d}) \propto L(\mathbf{x}|\mathbf{d})p(\mathbf{x}) \quad \text{(Eq. A.1)}$$

Where $\mathbf{d}$ contains the measurement data and $L(\mathbf{x}|\mathbf{d})$ and $p(\mathbf{x})$ denote the likelihood and prior distribution of $\mathbf{x}$, respectively. The used MCMC sampler is DREAM_{ZS} (Vrugt et al., 2009; Laloy and Vrugt, 2012). For brevity we describe herein only the differences with the approach proposed by Laloy et al. (2017) and refer the reader to this study for more details about the general methodology.

Our data vector, $\mathbf{d}$, contains the 4 concentrations measurements (two depths × 2 concentrations, ^{10}Be and ^{26}Al) and 2 concentration ratios (one $^{26}Al/^{10}Be$ ratio per depth) listed in Table 4 and Table 5. Also, note that Eq. 3 has to be solved separately for each of the 4 concentrations because the associated parameters in $\mathbf{x}$ are different for each depth and nuclide.

Assuming that the residual errors follow a normal distribution with zero mean, the likelihood function is given by

$$L(\mathbf{x}|\mathbf{d}) = \frac{1}{2\pi^{N/2}\det(\mathbf{\Sigma})^{1/2}} \exp\left\{-\frac{1}{2}[\mathbf{d} - F(\mathbf{x})]^{\mathrm{T}}\mathbf{\Sigma}^{-1}[\mathbf{d} - F(\mathbf{x})]\right\} \quad \text{(Eq. A.2)}$$

Where N is the number of measurement data ($N = 6$ herein), $\mathbf{\Sigma}$ is the error covariance matrix, $\det(\mathbf{\Sigma})$ denotes the determinant of $\mathbf{\Sigma}$, and $F(\mathbf{x})$ represents the vector of predictions corresponding to $\mathbf{d}$. Here we further assumed that the residual errors are uncorrelated, which means that $\mathbf{\Sigma}$ is a diagonal matrix with σ_i as diagonal elements and $\det(\mathbf{\Sigma}) = \prod_{i=1}^{N} \sigma_i^2$. For the 4 concentration measurements, we set σ_i to the corresponding analytical measurement errors (see 6th and 10th columns of Table 4) while the σ_i for the concentration ratios were derived by simple uncertainty propagation (see Table 5).

The prior pdf is a key element of Bayesian inference. This distribution encodes the available prior information about the parameters and balances the effect of the likelihood function on the posterior pdf (Eq. A.1). The prior distribution is especially influential in the case of relatively low information content of the measurement data (small number of data points and/or larger measurement errors). We assumed the individual prior parameter pdfs to be independent.

$$p(\mathbf{x}) = \prod_{i=1}^{8N_p} p(x_i) \quad \text{(Eq. A.3)}$$

with $N_p = 8$ the dimension of $\mathbf{x}$.

8 Acknowledgements

Seismology and Gravimetry section of the Royal Observatory of Belgium is acknowledged for the paleoseismologic investigation on the Rauw fault. SCR Sibelco and Leon Clemens are thanked respectively as owner and farmer of the terrain where the trench was excavated. OSL research at Ghent University (DV and JDG) is funded through the Fund for Scientific Research Flanders (FWO-Vlaanderen). We thank A.-E. Debeer (Ghent University) for technical assistance (OSL) and Christoph Burow (University of Cologne) to perform the ESR measurements. This work is performed in close cooperation with, and with the financial support of NIRAS/ONDRAF, the Belgian Agency for Radioactive Waste and Fissile Materials, as part of the programme on geological disposal of high-level/long-lived radioactive waste that is carried out by ONDRAF/NIRAS.

9 References

Adamiec, G., Aitken, M.J., 1998. Dose-rate conversion factors: update. Ancient TL 16, 37-50.

Aitken, M.J., 1976. Thermoluminescence age evaluation and assessment of error limits: revised system. Archaeometry 18, 233-238.

Aitken, M.J., 1985. Thermoluminescence Dating. Academia press, London, 359 pp.

Aitken, M.J., Alldred, J.C., 1972. The assessment of error limits in thermoluminescence dating. Archaeometry 14, 257-267.

Balco, G., Rovey, C.W., 2008. An isochron method for cosmogenic-nuclide dating of buried soils and sediments. American Journal of Science 308, 1083–1114. doi:10.2475/10.2008.02.

Bartz M., Duval M., Brill D., Zander A., King G.E., Rhein A., Walk J., Stauch G., Lehmkuhl F., Brückner H. (this volume). Testing the potential of K-feldspar postIR-IRSL and quartz ESR for dating coastal alluvial fan complexes in arid environments. Quaternary International.

Beerten, K., Rittner, S., Lomax, J., Radtke, U., 2008. Dose recovery tests using Ti-related ESR signals in quartz: First results. Quaternary Geochronology 3, 143–149. doi:10.1016/j.quageo.2007.05.002.

Beerten, K., Wemaere, I., Gedeon, M., Labat, S., Rogiers, B., Mallants, D., Salah, S., Leterme, B., 2010. Geological, hydrogeological and hydrological data for the Dessel disposal site. Project near surface disposal of category A waste at Dessel, NIROND–TR 2009–05 E V1, ONDRAF/NIRAS, Brussels.

Beerten, K., De Craen, M., Wouters, L., 2013. Patterns and estimates of post-Rupelian burial and erosion in the Campine area, north-eastern Belgium. Physics and Chemistry of the Earth 64, 12-20.

Beerten, K., Dreesen, R., Janssen, J., Van Uytven, D., 2018. The Campine Plateau. In: Demoulin, A. (Ed.), Landscapes and Landforms of Belgium and Luxembourg, World Geomorphological Landscapes, Springer International Publishing, pp. 193-214.

Berghmans, F., 2001. SCK•CEN Harwell Dosimeters Limited Red Perspex Dosimetry Exercise, Internal Report, INSTR/525/01-04, 2001.

Bøtter-Jensen, L., Andersen, L.E., Duller, G.A.T., Murray, A.S., 2003. Developments in radiation, stimulation and observation facilities in luminescence measurements. Radiation Measurements 37, 535-541.

Braucher, R., Merchel, S., Borgomano, J., Bourlès, D.L., 2011. Production of cosmogenic radionuclides at great depth: A multi-element approach. Earth and Planetary Science Letters 309, 1-9.

Brennan, B. J., 2003. Beta doses to spherical grains. Radiation Measurements 37, 299-303.

Chmeleff, J., von Blanckenburg, F., Kossert, K., Jakob, D., 2010. Determination of the 10Be half-life by multicollector ICP-MS and liquid scintillation counting. Nuclear Instruments and Methods in Physics Research B 263, 192–199.

Cloething, S.A.P.L., Ziegler, P.A., Bogaard, P.J.F., 30 co-workers and TOPO-EUROPE Working Group, 2007. TOPO-EUROPE: The geoscience of coupled deep Earth-surface processes. Global and Planetary Change 58, 1-118.

De Corte, F., Vandenberghe, D., De Wispelaere, A., Buylaert, J.-P., Van den haute, P., 2006. Radon loss from encapsulated sediments in Ge gamma-ray spectrometry for the annual radiation dose determination in luminescence dating. Czech Journal of Physics 56, D183-D194.

Dehnert, A., Kracht, O., Preusser, F., Akçar, N., Kemna, H.A., Kubik, P.W., Schlüchter, C., 2011. Cosmogenic isotope burial dating of fluvial sediments from the Lower Rhine Embayment, Germany, Quaternary Geochronology 6, 313-325.

Duller, G.A.T., 2003. Distinguishing quartz and feldspar in single grain luminescence measurements. Radiation Measurements 37, 161-165.

Dunai, T.J., 2010. Cosmogenic Nuclides: Principles, Concepts and Applications in the Earth Surface Sciences. Cambridge University Press, 198 pp. doi:10.1007/s13398-014-0173-7.2.

Duval, M., 2012. Dose response curve of the ESR signal of the Aluminum center in quartz grains extracted from sediment. Ancient TL 30, 41-50.

Duval, M., Guilarte, V., 2015. ESR dosimetry of optically bleached quartz grains extracted from Plio-Quaternary sediment: Evaluating some key aspects of the ESR signals associated to the Ti-centers. Radiation Measurements 78, 28–41. doi:10.1016/j.radmeas.2014.10.002.

Duval, M., Sancho, C., Calle, M., Guilarte, V., Peña-Monné, J.L., 2015. On the interest of using the multiple center approach in ESR dating of optically bleached quartz grains: Some examples from the Early Pleistocene terraces of the Alcanadre River (Ebro basin, Spain). Quaternary Geochronology 29, 58-69.

Gibbard, P.L., 2007. Europe cut adrift. Nature 448, 259-260.

Gosse, J., Klein, J., 2015. Terrestrial cosmogenic nuclide dating. In: Rink, W.J., Thompson, J.W. (Eds.), Encyclopedia of Scientific Dating Methods, Springer International Publishing, pp. 799-813.

Grün, R., 1989. ESR dating. Quaternary International 1, 65-109.

Guérin, G., Mercier, N., Adamiec, G., 2011. Dose-rate conversion factors: update. Ancient TL, 29, 5-8.

Gullentops, F., Wouters, L., 1996. Delfstoffen in Vlaanderen. Ministerie van de Vlaamse Gemeenschap, Departement EWBL, Brussel, 180 pp.

Gupta, S., Collier, J.S., Palmer-Felgate, A., Potter, G., 2007. Catastrophic flooding origin of shelf valley systems in the English Channel. Nature 448, 342–345.

Gupta, S., Collier, J.S., Garcia-Moreno, C., Oggioni, F., Trentesaux, A., Vanneste, K., De Batist, M., Camelbeeck, T., Potter, G., Van Vliet-Lanoë, B., Arthur, J.C.R., 2017. Two-stage opening of the Dover Strait and the origin of island Britain. Nature Communications 8, 15101. doi: 10.1038/ncomms15101

Heyse, I., Demoulin, A., 2018. The Flemish Valley: Response of the Scheldt Drainage System to Climatic and Glacio-Eustatic Oscillations. In: Demoulin, A. (Ed.), Landscapes and Landforms of Belgium and Luxembourg, World Geomorphological Landscapes, Springer International Publishing, pp. 297-311.

Hossain, S.M., 2003. A critical comparison and evaluation of methods for the annual radiation dose determination in the luminescence dating of sediments. PhD-thesis Universiteit Gent.

Kreutzer, S., Duval, M., Bartz, M., Bertran, P., Bosq, M., Eynaud, F., Verdin, F., Mercier, N., 2018. Deciphering long-term coastal dynamics using IR-RF and ESR dating: a case study from Médoc, south-west France. Quaternary Geochronology 48, 108-120.

Kubik, P.W., Christl, M., 2010. 10Be and 26Al measurements at the Zurich 6 MV Tandem AMS facility. Nuclear Instruments and Methods in Physics Research B 268, 880-883.

Lachner, J., Christl, M., Müller, A.M., Suter, M., Synal, H.-A., 2014. 10Be and 26Al low-energy AMS using He-stripping and background suppression via an absorber. Nuclear Instruments and Methods in Physics Research B 331, 209-214.Laga, P., Louwye, S., Geets, S., 2001. Paleogene and Neogene lithostratigraphic units (Belgium). Geologica Belgica 4, 135-152.

Laloy, E., Beerten, K., Vanacker, V., Christl, M., Rogiers, B., Wouters, L., 2017. Bayesian inversion of a CRN depth profile to infer Quaternary erosion of the northwestern Campine Plateau (NE Belgium). Earth Surface Dynamics 5, 331-345.

Laloy, E., Vrugt, J. A., 2012. High-dimensional posterior exploration of hydrologic models using multiple-try DREAM(ZS) and high-performance computing. Water Resources Research 48, W01526. doi:10.1029/2011WR010608.

Madsen, A.T., Murray, A.S., 2009. Optically stimulated luminescence dating of young sediments: a review. Geomorphology 109, 3-16.

Marrero, S., Phillips, F. M., Borchers, B., Lifton, N., Aumer, R., Balco, G., 2016. Cosmogenic nuclide systematics and the CRONUScalc program. Quaternary Geochronology 31, 160-187.

Miller, K.G., Kominz, M.A., Browning, J.V., Wright, J.D., Mountain, G.S., Katz, M.E., Sugarman, P.J., Cramer, B.S., Christie-Blick, N., Pekar, S.F., 2005. The Phanerozoic record of global sea-level change. Science 310, 1293-1298.

Murray, A.S., Olley, J.M., 2002. Precision and accuracy in the optically stimulated luminescence dating of sedimentary quartz: a status review. Geochronometria 21, 1-16.

Murray, A.S., Wintle, A.G., 2000. Luminescence dating of quartz using an improved single-aliquot regenerative-dose protocol. Radiation Measurements 32, 57-73.

Murray, A.S., Wintle, A.G., 2003. The single aliquot regenerative dose protocol: potential for improvements in reliability. Radiation Measurements 37, 377-381.

Norris, T.L., Gancarz, A.J., Rokop, D.J., Thomas, K.W., 1983. Half-life of Al-26. Journal of Geophysical Research 88, B331-B333.

Norton, K.P., Vanacker, V., 2009. Effects of terrain smoothing on topographic shielding correction factors for cosmogenic nuclide-derived estimates of basin-averaged denudation rates. Earth Surface Processes and Landforms 34, 146-154.

Portenga, E. W., Bierman, P. R., 2011. Understanding Earth's eroding surface with 10Be, GSA Today, 21, 4–10.

Prescott, J.R., Hutton, J.T., 1994. Cosmic ray contributions to dose rates for luminescence and ESR dating: large depths and long-term time variations. Radiation Measurements 23, 497-500.

Rhodes, E.J., 2011. Optically Stimulated Luminescence Dating of Sediments over the Past 200,000 Years. Annual Review of Earth and Planetary Sciences 39, 461–88.

Rixhon, G., Briant, R.M., Cordier, S., Duval, M., Jones, A., Scholz, D., 2017. Revealing the pace of river landscape evolution during the Quaternary: recent developments in numerical dating methods. Quaternary Science Reviews 166, 91-113.

Rixhon, G., Demoulin, A., 2018. The Picturesque Ardennian Valleys: Plio-Quaternary Incision of the Drainage System in the Uplifting Ardenne. In: Demoulin, A. (Ed.), Landscapes and Landforms of Belgium and Luxembourg, World Geomorphological Landscapes, Springer International Publishing, pp. 159-175.

Schellmann, G., Beerten, K., Radtke, U., 2008. Electron spin resonance (ESR) dating of Quaternary materials. E&G Quaternary Science Journal 57, 150-178.

Schokker, J., Cleveringa, P., Murray, A.S., Wallinga, J., Westerhoff, W.E., 2005. An OSL dated Middle and Late Quaternary sedimentary record in the Roer Valley Graben (southeastern Netherlands). Quaternary Science Reviews 24, 2243–2264. doi:10.1016/j.quascirev.2005.01.010

Stone, J.O., 2000. Air pressure and cosmogenic isotope production. Journal of Geophysical Research 105, 23753.

Tavernier, R., De Moor, G., 1974. L'évolution du Bassin de l'Escaut. In: Macar, P., Gullentops, F., Pissart, A., Tavernier, R., Zonneveld, J.I.S. (Eds.), L'évolution Quaternaire des bassins fluviaux de la mer du nord méridionale, Centenaire Société Géologique de la Belgique, Liège, pp. 159-233.

Timar-Gabor, A., Vasiliniuc, Ş., Vandenberghe, D.A.G., Cosma, C., Wintle, A.G., 2012. Investigations into the reliability of SAR-OSl equivalent doses obtained for quartz samples displaying dose response curves with more than one component. Radiation Measurements 47, 740-745.

Timar-Gabor, A., Wintle, A.G., 2013. On natural and laboratory generated dose response curves for quartz of different grains sizes from Romanian loess. Quaternary Geochronology 18, 34-40.

Toucanne, S., Zaragosi, S., Bourillet, J.F., Gibbard, P.L., Eynaud, F., Giraudeau, J., Turon, J.L., Cremer, M., Cortijo, E., Martinez, P., Rossignol, L., 2009. A 1.2 Ma record of glaciation and fluvial discharge from the Western European Atlantic margin. Quaternary Science Reviews 28, 2974-2981.

Toyoda, S., Voinchet, P., Falguères, C., Dolo, J.M., Laurent, M., 2000. Bleaching of ESR signals by the sunlight: a laboratory experiment for establishing the ESR dating of sediments. Applied Radiation and Isotopes 52, 1357-1362.

Vanacker, V., von Blanckenburg, F., Hewawasam, T., Kubik, P.W., 2007. Constraining landscape development of the Sri Lankan escarpment with cosmogenic nuclides in river sediment. Earth and Planetary Science Letters 253, 402-414.

Vandenberghe, D., 2004. Investigation of the optically stimulated luminescence dating method for application to young geological sediments. PhD-thesis Universiteit Gent: 298 pp.

Vandenberghe, D., Kasse, C., Hossain, S.M., De Corte, F., Van den haute, P., Fuchs, M., Murray, A.S., 2004. Exploring the method of optical dating and comparison of optical and 14C ages of Late Weichselian coversands in the southern Netherlands. Journal of Quaternary Science 19, 73-86.

Vandenberghe, D., De Corte, F., Buylaert, J.-P., Kučera, J., Van den haute, P., 2008. On the internal radioactivity in quartz. Radiation Measurements 43, 771-775.

Vandenberghe, J., De Smedt, P., 1979. Palaeomorphology in the eastern Scheldt basin (Central Belgium) - The dijle-demer-grote nete confluence area. Catena 6, 73-105.

Vandenberghe, N., Van Simaeys, S., Steurbaut, E., Jagt, J.W.M., Felder, P.J., 2004. Stratigraphic architecture of the Upper Cretaceous and Cenozoic along the southern border of the North Sea Basin in Belgium. Netherlands Journal of Geosciences 83, 155-171.

Vanneste, K., Camelbeeck, T., Verbeeck, K., 2013. A Model of Composite Seismic Sources for the Lower Rhine Graben, Northwest Europe. Bulletin of the Seismological Society of America 103, 984-1007. doi: http://dx.doi.org/10.1785/0120120037.

Verbeeck, K., Wouters, L., Vanneste, K., Camelbeeck, T., Vandenberghe, D., Beerten, K., Rogiers, B., Schiltz, M., Burow, C., Mees, P., De Grave, J., Vandenberghe, N., 2017. Episodic activity of a dormant fault in tectonically stable Europe : the Rauw fault (NE Belgium). Tectonophysics 699, 146-163.

Vernes, R.W., Deckers, J., Bakker, M.A.J., Bogemans, F., De Ceukelaire, M., Doornenbal, J.C., den Dulk, M., Dusar, M., Van Haren, T.F.M., Heyvaert, V.M.A., Kiden, P., Kruisselbrink, A.F., Lanckacker, T., Menkovic, A., Meyvis, B., Munsterman, D.K., Reindersma, R., ten Veen, J.H., van de Ven, T.J.M., Walstra, J., Witmans, N., 2018. Geologisch en hydrogeologisch 3D model van het Cenozoïcum van de Belgisch-Nederlandse grensstreek van Midden-Brabant / De Kempen (H3O – De Kempen). Studie uitgevoerd door VITO, TNO-Geologische Dienst Nederland en de Belgische Geologische Dienst in opdracht van Vlaams Planbureau voor Omgeving, Vlaamse Milieumaatschappij, TNO, Geologische Dienst Nederland, Nederlandse Provincie Noord-Brabant, Brabant Water, Programmabureau KRW/DHZ Maasregio.

Voinchet, P., Falguères, C., Laurent, M., Toyoda, S., Bahain, J.J. and Dolo, J.M., 2003. Artificial optical bleaching of the Aluminium center in quartz : implications to ESR dating of sediments. Quaternary Science Reviews 22, 1335-1338.

Voinchet, P., Falguères, C., Tissoux, H., Bahain, J.J., Despriée, J., Pirouelle, F., 2007. ESR dating of fluvial quartz: Estimate of the minimal distance transport required for getting a maximum optical bleaching. Quaternary Geochronology 2, 363–366. doi:10.1016/j.quageo.2006.04.010.

Voinchet, P., Toyoda, S., Falguères, C., Hernandez, M., Tissoux, H., Moreno, D., Bahain, J.-J., 2015. Evaluation of ESR residual dose in quartz modern samples, an investigation on environmental dependence. Quaternary Geochronology 30, 506–512. doi:10.1016/j.quageo.2015.02.017.

von Blanckenburg, F., Belshaw, N. S., O'Nions, R. K., 1996. Separation of 9Be and cosmogenic 10Be from environmental materials and SIMS isotope dilution analysis. Chemical Geology 129, 93-99.

Vrugt, J. A., Braak, C. J. F. T., Diks, C. G. H., Robinson, B. A., Hyman, J. M., Higdon, D., 2009. Accelerating Markov chain Monte Carlo simulation by differential evolution with self-adaptive randomized subspace sampling. International Journal of Nonlinear Sciences and Numerical Simulation 10, 273–290.

Westerhoff, W.E., Wong, T.E., Geluk, M.C., 2003. Opbouw van de ondergrond. In: De Mulder, E.F.J., Geluk, M.C., Ritsema, I., Westerhoff, W.E., Wong, T.E. (Eds), De ondergrond van Nederland, Wolters-Noordhoff, Groningen/Houten, pp. 247-352.

Westerhoff, W.E., Kemna, H.A., Boenigk, W., 2008. The confluence area of Rhine, Meuse, and Belgian rivers: Late Pliocene and Early Pleistocene fluvial history of the northern Lower Rhine Embayment. Netherlands Journal of Geosciences 87, 107–125.

Wintle, A.G., 2008. Luminescence dating of Quaternary sediments - introduction. Boreas 37, 469-470.

Wintle, A.G., Murray, A.S., 2006. A review of quartz optically stimulated luminescence characteristics and their relevance in single-aliquot regeneration dating protocols. Radiation Measurements 41, 369-391.

Woda, C., Wagner, G.A., 2007. Non-monotonic dose dependence of the Ge- and Ti-centres in quartz. Radiation Measurements 42, 1441-1452.

Figure 1 – (a) Location of the Campine area in western Europe. (b) Topographical map of the Belgian-Dutch-German border region, showing the main Roer Valley Graben faults, the Brabant and Rhenohercynian Massifs, the Campine Basin, the outline of the Flemish Valley and the location of the Nete catchment. Also indicated is the former course of the rivers Rhine and Meuse, and the presumed direction of headwards erosion that created the Flemish Valley and the Nete catchment as its extension. The small shaded rectangle refers to Figure 3.

Figure 2 – Chronostratigraphy and lithostratigraphy of formations and members mentioned in the text (based on Vernes et al. (2018), Vandenberghe et al. (2004), Westerhoff et al. (2008), Schokker et al. (2005) and this study).

Figure 3 – Geological cross-section through the study area with indication of the different lithostratigraphical units and the approximate position of the Rauw fault in Postel, municipality of Mol (Verbeeck et al., 2017; Vernes et al., 2018). The Postel trench and the MHR quarry (Laloy et al., 2017) are indicated with a black dot. DI = Diest Formation, KL = Kasterlee Formation, KI = Kiezelooliet Formation, SY = Stramproy Formation, ST = Sterksel Formation, BX = Boxtel Formation, Mol = Mol Formation, Gent = Gent Formation.

Figure 4 – Schematic cross-section of the trench with indication of the different lithological units, the ESR-OSL-CRN samples and the Rauw fault (Verbeeck et al., 2017). Unit A1: well sorted, well rounded medium to coarse white quartz sand with vague horizontal layering; unit A2: black detrital organic-rich sand; unit A3: the same quartz sand as in unit A1, but coated with organic material, which gives it a distinct brown colour; unit A4: idem as unit A3 but with steep north-east dipping foresets; unit B: greenish loamy sand, featuring cryoturbations and relict ice-wedges; unit C: coarse sand with some gravel; unit D-E-F: slightly loamy fine-grained sand with illuviation horizons and ploughed at the top.

Figure 5 – Bleaching curves for various ESR centres. (a) Sample GLL-153103. (b) Sample GLL-153104.

Figure 6 – Dose response curves. (a) Ti centre, sample GLL-153103. (b) Ti centre, sample GLL-153104. (c) Ti-Li centre, sample GLL-153103. (d) Ti-Li centre, sample GLL-153104. (e) Al-centre, sample GLL-153103. (f) Al-centre, sample GLL-153104. DSE* = double saturating exponential with opposite sign; DSE = double saturating exponential.

Figure 7 – (a) Dependence of equivalent dose (ED) on preheat temperature for sample GLL-153103. (b) Idem for sample GLL-153104. (c) Corresponding recycling and OSL IR depletion ratios, and values for recuperation, for sample GLL-153103. (d) Idem for sample GLL-153104. Data represent the average (± 1 standard error) of at least three replicate measurements.

Figure 8 – SAR dose-response curve for an aliquot of sample GLL-153103 (obtained using a preheat of 10 s at 220°C). The recycling point is shown as an open circle. The solid line is the fit of the data to

the sum of two saturating exponential functions. The equivalent dose is obtained by interpolation of the sensitivity-corrected natural OSL signal (open square) on the corrected growth-curve.

Figure 9 – Posterior distributions (blue histograms) and associated priors (red lines). (a) Total burial age for sample GLL-153103. (b) Total burial age for sample GLL-153104. (c) Initial burial depth for sample 3103. (d) Initial burial depth for sample 3104. (e) Erosion rate for sample 3103. (f) Erosion rate for sample 3103. (g) Surface exposure age for sample 3103. (h) Surface exposure age for sample 3104. (i) Inherited ^{10}Be concentration for samples -03 and -04. (j) Inherited ^{26}Al concentration for samples -03 and -04.

Figure 10 –Schematized revised burial-erosion history of the western edge of the Campine Plateau. See Figure 3 for the location and approximate horizontal scale of the cross-section. MOL/SY = Mol/Stramproy Formation; ST = Sterksel Formation (Lommel Sands). (a) Late Pliocene to earliest Pleistocene deposition of sampled sediment, in any case prior to ca. 1.5 Ma. (b) Build-up of sediment column until ca. 1 Ma at the latest (mean value 1.55 ± 0.80 Ma). (c) Rauw fault activation around 1 Ma (and probably even earlier) following weak erosion. (d) Deposition of the fluvial (Rhine) Lommel Sands (Sterksel Formation) between 1 Ma and 0.5 Ma in the east while weak erosion continues in the west. (e) Strong erosion starting around 0.5 Ma results in the present-day topography. Black dots indicate the altitude of the present-day surface. Red triangles indicate the position of the samples.

Table 1 – Sample details.

ESR/OSL sample code	*CRN lab code (resp. $^{10}Be/^{26}Al$)*	*Latitude (dd)*	*Longitude (dd)*	*Altitude (m T.A.W.)*	*Depth (cm)*
GLL-153103	TB2343/ZA1902	51.2483	5.1994	36.8	164
GLL-153104	TB2344/ZA1903	51.2483	5.1994	36.8	248

Table 1 – Radionuclide concentrations used for dose rate evaluation, estimates of past gravimetric water content (w.c.) and calculated dose rates. The total dose rate includes the contributions of internal radioactivity (f_i), external beta radiation (f_β), external gamma irradiation (f_γ) and cosmic rays (f_c). The uncertainties mentioned with the dosimetry data are random. All uncertainties represent 1σ.

GLL-code	*^{40}K (Bq kg^{-1})*	*^{234}Th (Bq kg^{-1})*	*^{226}Ra (Bq kg^{-1})*	*^{210}Pb (Bq kg^{-1})*	*^{232}Th (Bq kg^{-1})*	*w.c. (%)*	f_i	f_β	f_γ	f_c	*Total dose rate (Gy ka^{-1})*
GLL-153103	3.9 ± 0.4	1.5 ± 0.6	2.2 ± 0.2	1.9 ± 0.5	2.2 ± 0.1	24 ± 1	0.07	0.32	0.38	0.23	0.19 ± 0.01
GLL-153104	2.4 ± 0.4	2.2 ± 0.6	2.0 ± 0.2	1.9 ± 0.6	1.2 ± 0.1	24 ± 1	0.08	0.34	0.33	0.25	0.16 ± 0.01

Table 2 – ESR and OSL dating results. ESR uncertainties are calculated from propagating individual random uncertainties for equivalent dose (fitting error) and dose rate. The following fitting functions are used: DSE* (double saturating exponential with opposite sign), SSE (single saturating exponential), DSE (double saturating exponential) and SSE+LIN (single saturating exponential plus linear). Only dose points below 10 kGy were used for fitting the SSE function to the dose points. Uncertainties on the luminescence ages were determined according to the error assessment system proposed by Aitken and Alldred (1972) and Aitken (1976); summarized in Aitken (1985). Additional information on the different sources of systematic uncertainty and their quantification can be found in Vandenberghe et al. (2004; see also Vandenberghe, 2004). All uncertainties represent 1σ.

Sample	*ESR*				*OSL*	
	Centre	*Fitting method*	*D_e (10^3 Gy)*	*Age (Ma)*	*D_e (10^3 Gy)*	*Age (Ma)*
GLL-153103	Ti	DSE*	1.04 ± 0.27	5.5 ± 1.4	0.260 ± 0.017	1.4 ± 0.2
	Ti	SSE	0.85 ± 0.41	4.5 ± 2.2		
	Ti-Li	DSE*	2.43 ± 0.53	12.8 ± 2.9		
	Ti-Li	SSE	2.21 ± 0.28	11.6 ± 1.5		
	Al	DSE	1.95 ± 0.41	10.3 ± 2.2		
	Al	SSE+LIN	1.95 ± 0.25	10.3 ± 1.4		
GLL-153104	Ti	DSE*	0.76 ± 0.31	4.8 ± 2.0	0.246 ± 0.014	1.6 ± 0.2
	Ti	SSE	0.76 ± 0.28	4.8 ± 1.8		
	Ti-Li	DSE*	0.87 ± 0.25	5.4 ± 1.6		
	Ti-Li	SSE	0.75 ± 0.22	4.7 ± 1.4		
	Al	DSE	2.14 ± 0.27	13.4 ± 1.9		
	Al	SSE+LIN	1.91 ± 0.35	11.9 ± 2.3		

Table 3 – Analytical results of the cosmogenic radionuclide analysis. Errors are given at 1 sigma level.

Sample	*Quartz (g)*	*^{9}Be carrier (g)*	*^{10}Be/^{9}Be (-)*	*^{10}Be (at./g qtz)*	*Total error ^{10}Be (at./g qtz)*	*^{27}Al total (g)*	*^{26}Al/^{27}Al (-)*	*^{26}Al (at./g qtz)*	*Total ^{26}Al error (at./g qtz)*
GLL-153103	9.02	1.52E-04	4.91E-14	5.31E+04	6.03E+03	1.11E-03	8.52E-14	2.28E+05	7.50E+04
GLL-153104	11.34	1.52E-04	5.73E-14	4.96E+04	3.91E+03	1.29E-03	7.52E-14	1.85E+05	6.36E+04

Table 4 – Simple burial ages based on the ^{26}Al/^{10}Be ratio of the samples (1σ). These should be regarded as minimum ages.

Sample	*^{26}Al/^{10}Be*	*Burial age (Ma)*
GLL-153103	4.30 ± 1.50	0.9 ± 0.7
GLL-153104	3.73 ± 1.32	1.2 ± 0.8

Table 5 – Posterior distribution statistics for 2 sampled variables: the time since the start of erosion, t_E, and the erosion rate, *E.* The ranges encompass the central 68% of the posterior distribution, for the sake of comparison with the data in Table 2 and Table 4.

Sample	*median E (m/Ma)*	*range E (m/Ma)*	*median t_E (Ma)*	*range t_E (Ma)*
GLL-153103	15 ± 8	10-30	1.4 ± 0.7	0.6-2.6
GLL-153104	13 ± 9	8-30	1.7 ± 0.9	0.7-3.1

Table 7 – Summary of the ESR, OSL and CRN ages. Errors are given at 1 sigma level.

Sample	*ESR age (Ma)*	*OSL age (Ma)*	*CRN, median t_E (Ma)*
GLL-153103	4.5 ± 2.2	1.4 ± 0.2	1.4 ± 0.7
GLL-153104	4.8 ± 1.8	1.6 ± 0.2	1.7 ± 0.9

Figure 01

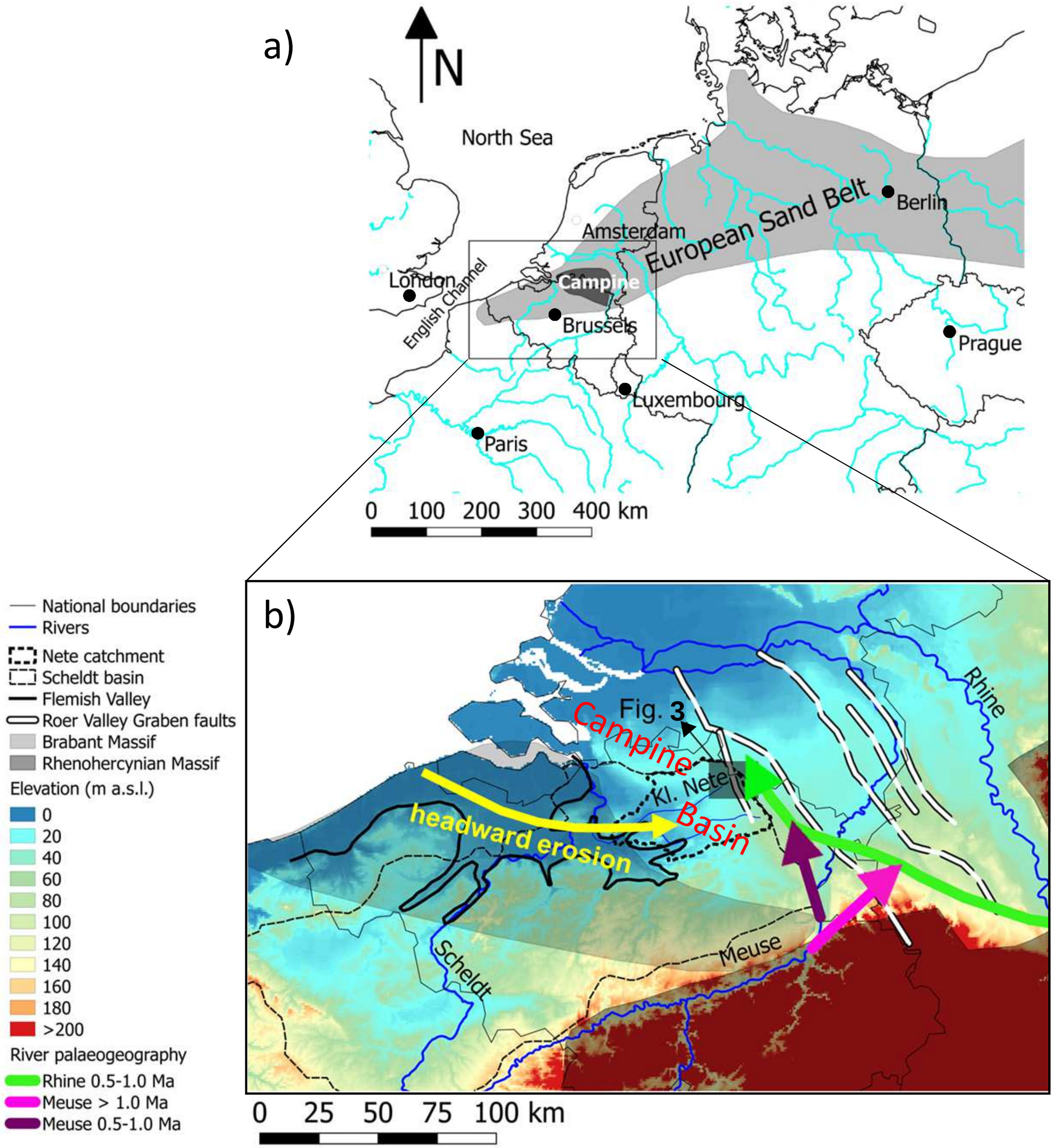
a)
N
North Sea
European Sand Belt
Berlin
Amsterdam
London
English Channel
Campine
Brussels
Prague
Luxembourg
Paris
0 100 200 300 400 km
b)
National boundaries
Rivers
Nete catchment
Scheldt basin
Flemish Valley
Roer Valley Graben faults
Brabant Massif
Rhenohercynian Massif
Elevation (m a.s.l.)
0
20
40
60
80
100
120
140
160
180
>200
River palaeogeography
Rhine 0.5-1.0 Ma
Meuse > 1.0 Ma
Meuse 0.5-1.0 Ma
Fig. 3
Campine
Basin
Kl. Nete
headward erosion
Rhine
Meuse
Scheldt
0 25 50 75 100 km

Figure 02

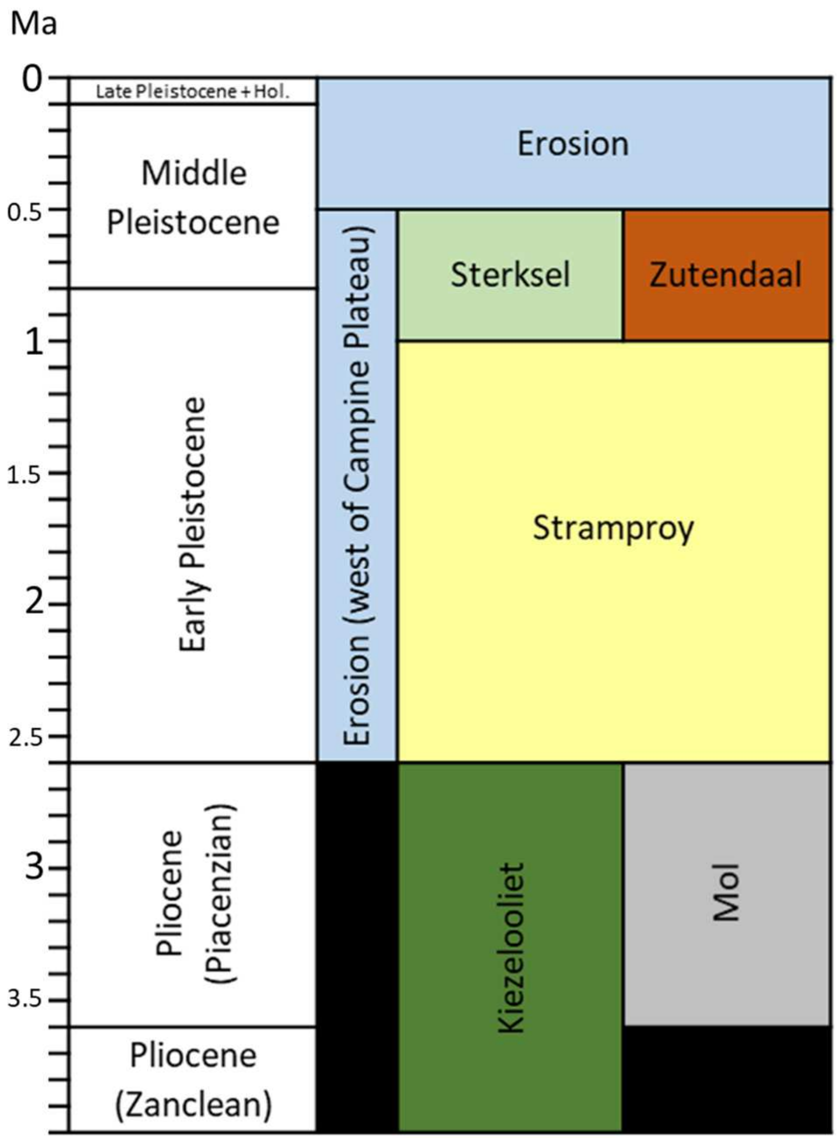
Ma
0
0.5
1
1.5
2
2.5
3
3.5
Late Pleistocene + Hol.
Middle Pleistocene
Early Pleistocene
Pliocene (Piacenzian)
Pliocene (Zanclean)
Erosion
Erosion (west of Campine Plateau)
Sterksel
Zutendaal
Stramproy
Kiezelooliet
Mol

Figure 03

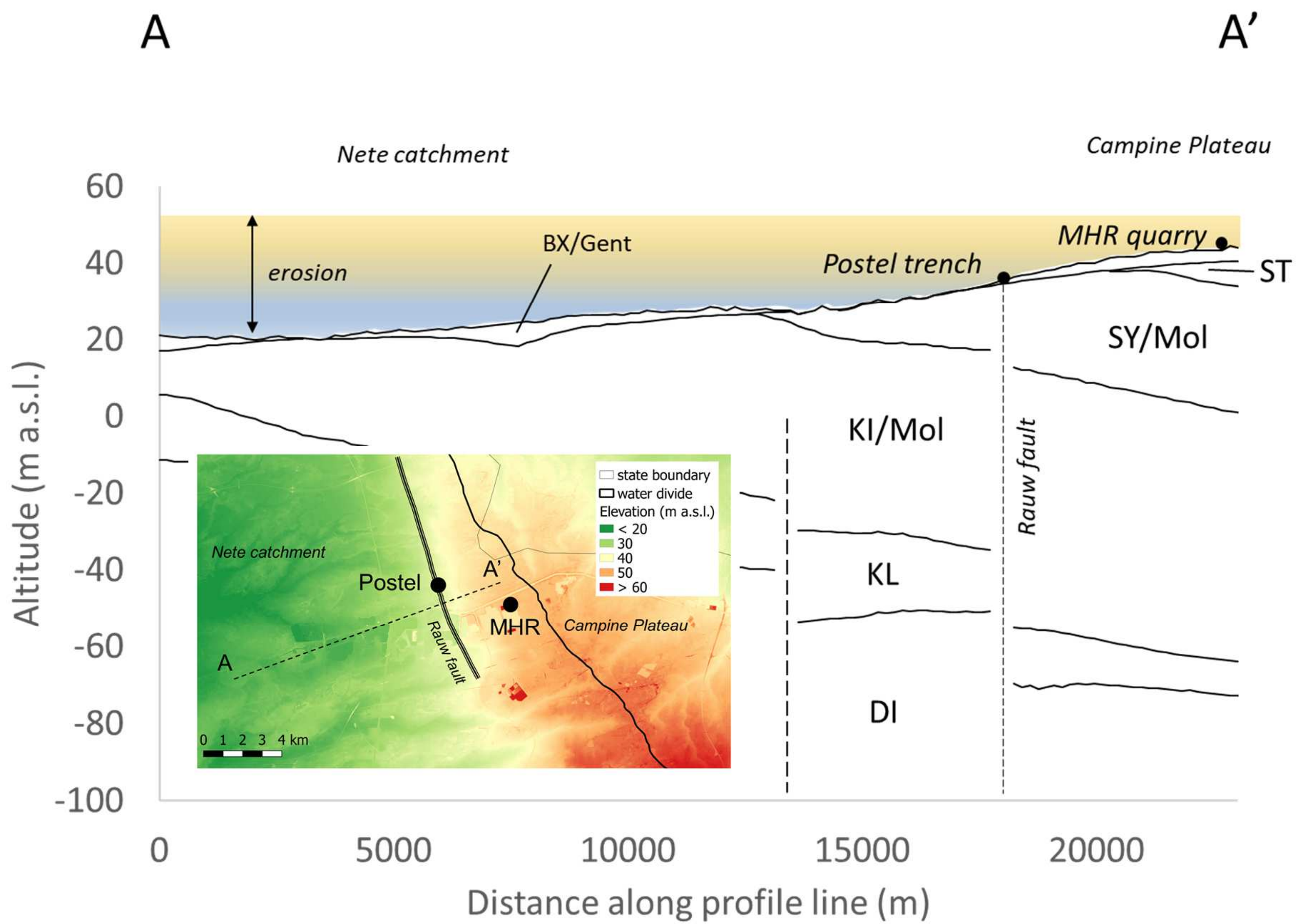
A
A'
Nete catchment
Campine Plateau
60
40
20
0
-20
-40
-60
-80
-100
Altitude (m a.s.l.)
erosion
BX/Gent
Postel trench
MHR quarry
ST
SY/Mol
Kl/Mol
KL
Dl
Rauw fault
0
5000
10000
15000
20000
Distance along profile line (m)
state boundary
water divide
Elevation (m a.s.l.)
< 20
30
40
50
> 60
Nete catchment
Postel
A'
MHR
Campine Plateau
A
Rauw fault
0 1 2 3 4 km

Figure 04

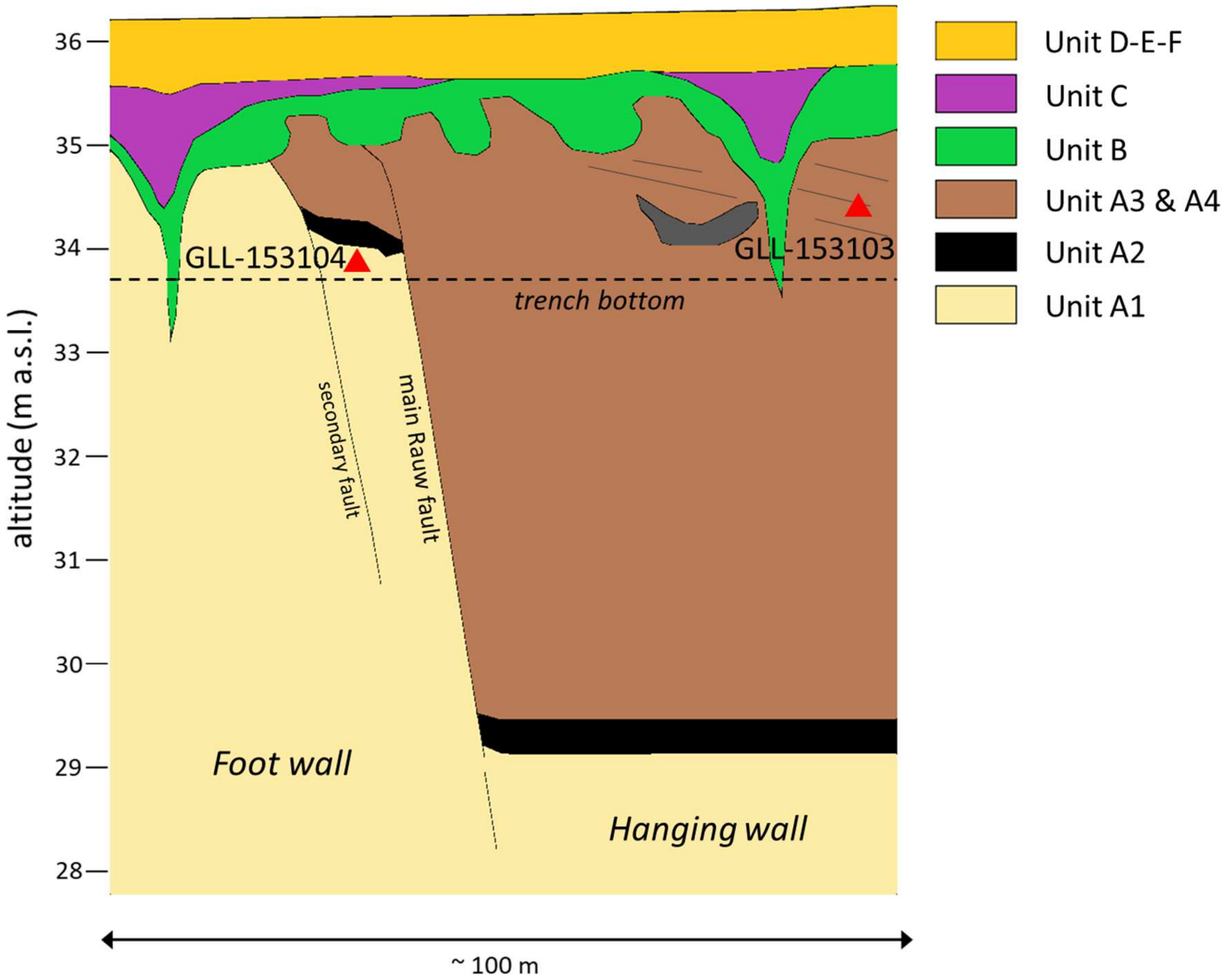
36
35
34
33
32
31
30
29
28
altitude (m a.s.l.)
GLL-153104
GLL-153103
trench bottom
secondary fault
main Rauw fault
Foot wall
Hanging wall
~ 100 m
Unit D-E-F
Unit C
Unit B
Unit A3 & A4
Unit A2
Unit A1

Figure 05

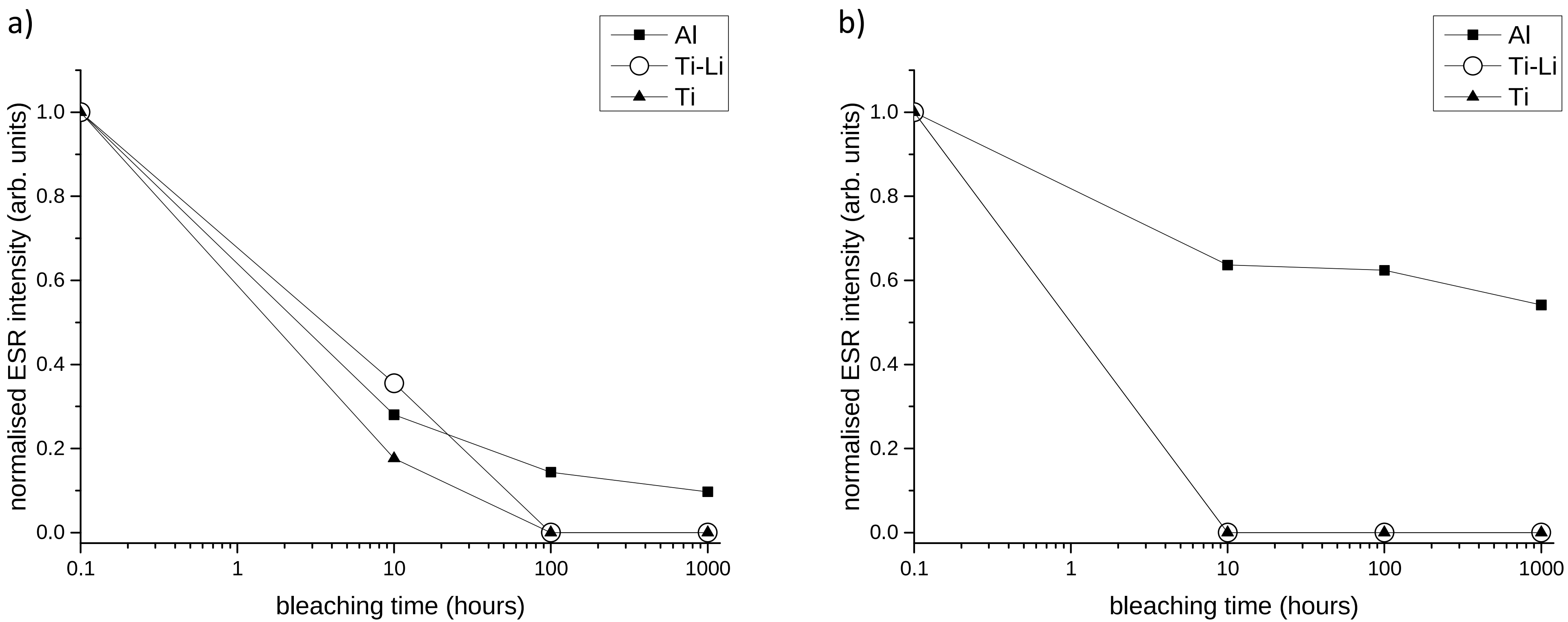
a)
Al
Ti-Li
Ti
normalised ESR intensity (arb. units)
1.0
0.8
0.6
0.4
0.2
0.0
0.1
1
10
100
1000
bleaching time (hours)
b)
Al
Ti-Li
Ti
normalised ESR intensity (arb. units)
1.0
0.8
0.6
0.4
0.2
0.0
0.1
1
10
100
1000
bleaching time (hours)

Figure 06

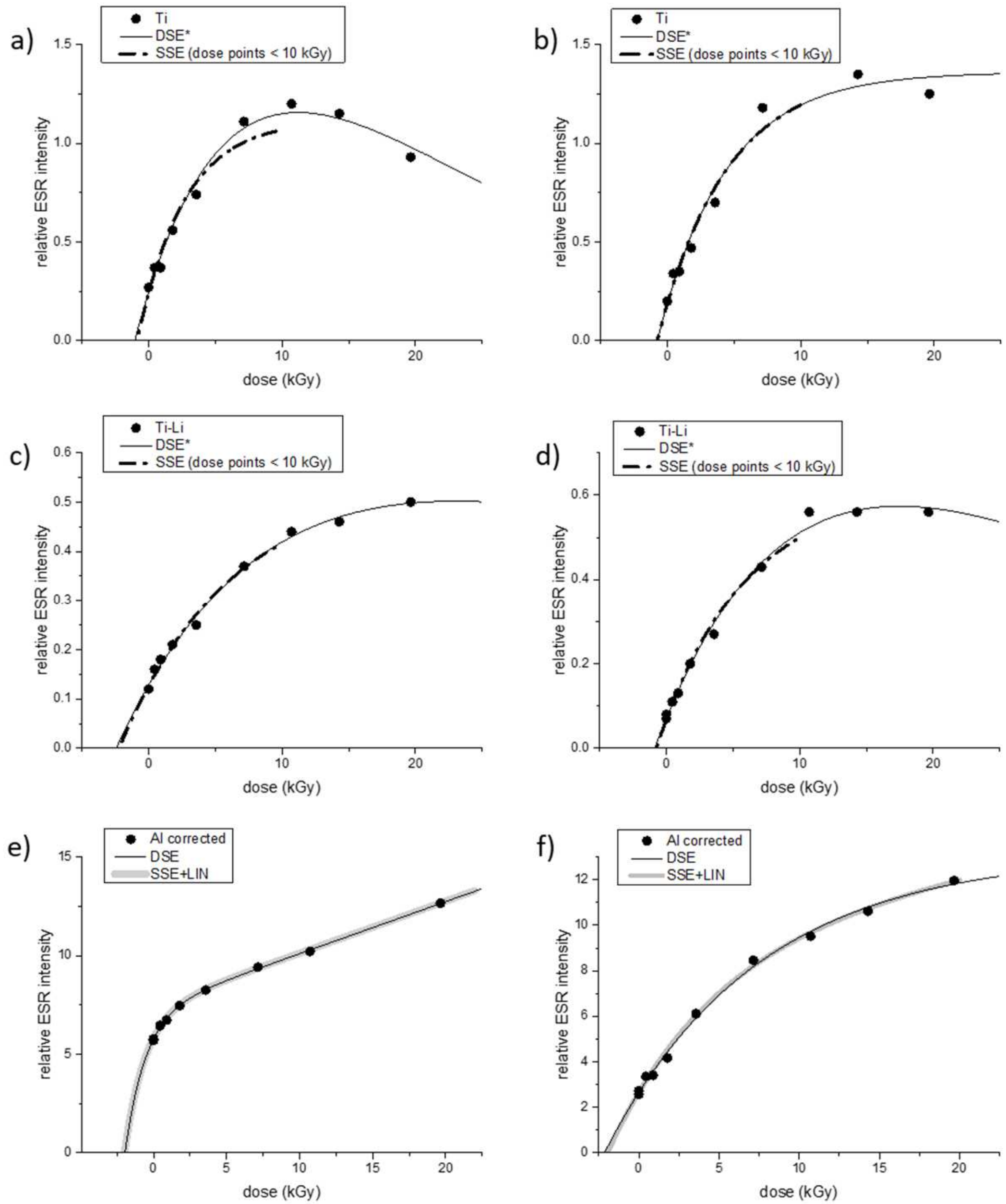
a)
Ti
DSE*
SSE (dose points < 10 kGy)
relative ESR intensity
dose (kGy)
b)
Ti
DSE*
SSE (dose points < 10 kGy)
relative ESR intensity
dose (kGy)
c)
Ti-Li
DSE*
SSE (dose points < 10 kGy)
relative ESR intensity
dose (kGy)
d)
Ti-Li
DSE*
SSE (dose points < 10 kGy)
relative ESR intensity
dose (kGy)
e)
Al corrected
DSE
SSE+LIN
relative ESR intensity
dose (kGy)
f)
Al corrected
DSE
SSE+LIN
relative ESR intensity
dose (kGy)

Figure 07

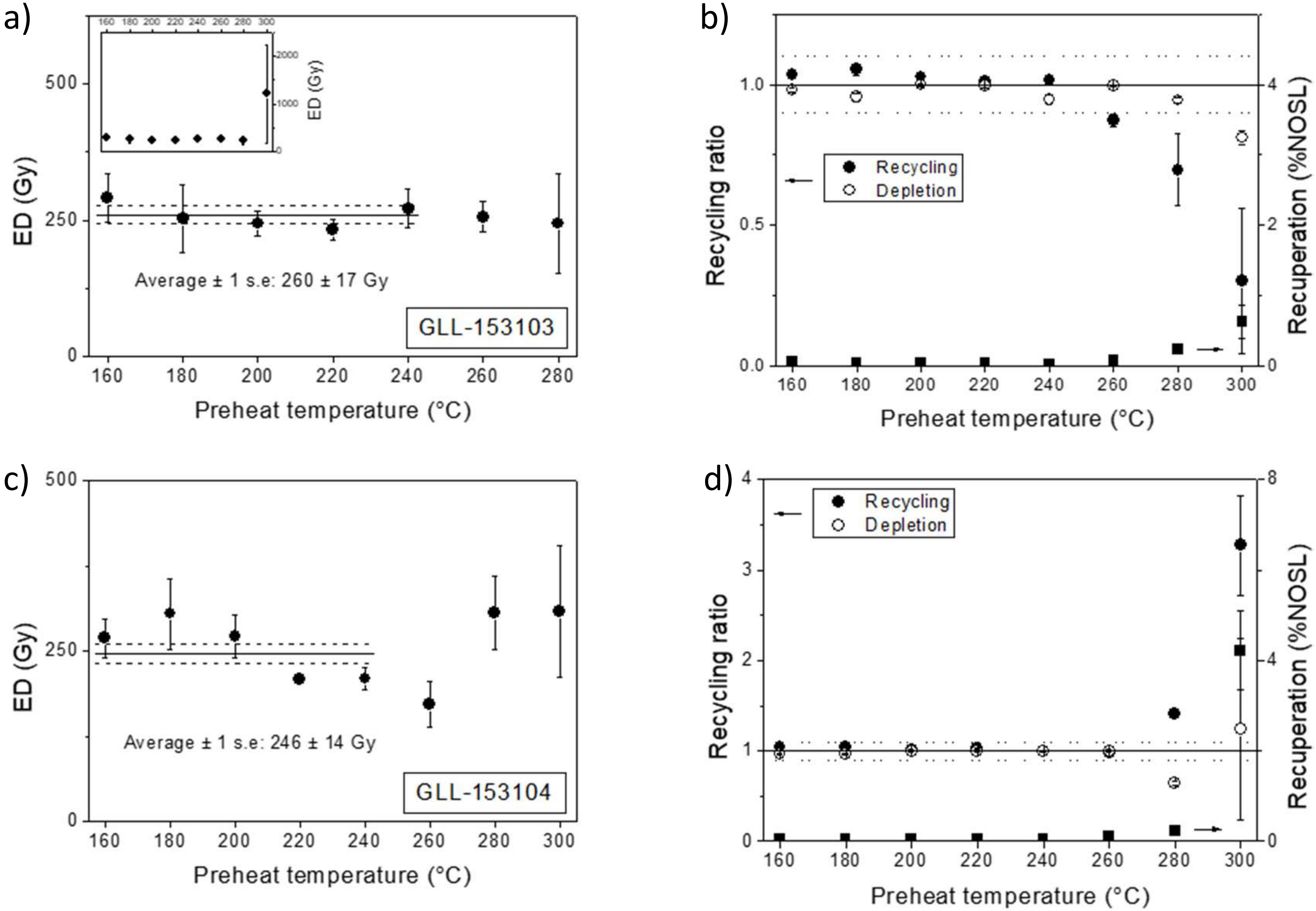
a)
ED (Gy)
Preheat temperature (°C)
Average ± 1 s.e: 260 ± 17 Gy
GLL-153103
b)
Recycling ratio
Recuperation (%NOSL)
Recycling
Depletion
Preheat temperature (°C)
c)
ED (Gy)
Average ± 1 s.e: 246 ± 14 Gy
GLL-153104
Preheat temperature (°C)
d)
Recycling ratio
Recuperation (%NOSL)
Recycling
Depletion
Preheat temperature (°C)

Figure 08

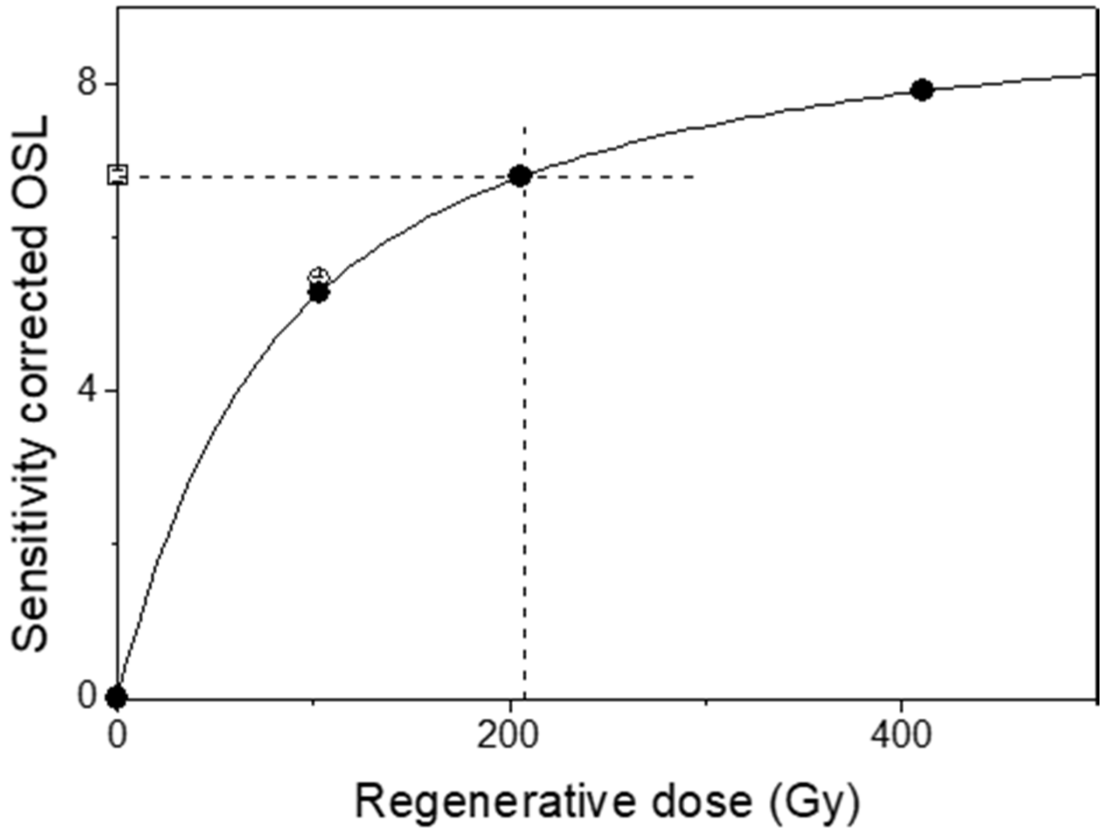
8
4
0
0
200
400
Sensitivity corrected OSL
Regenerative dose (Gy)

Figure 09

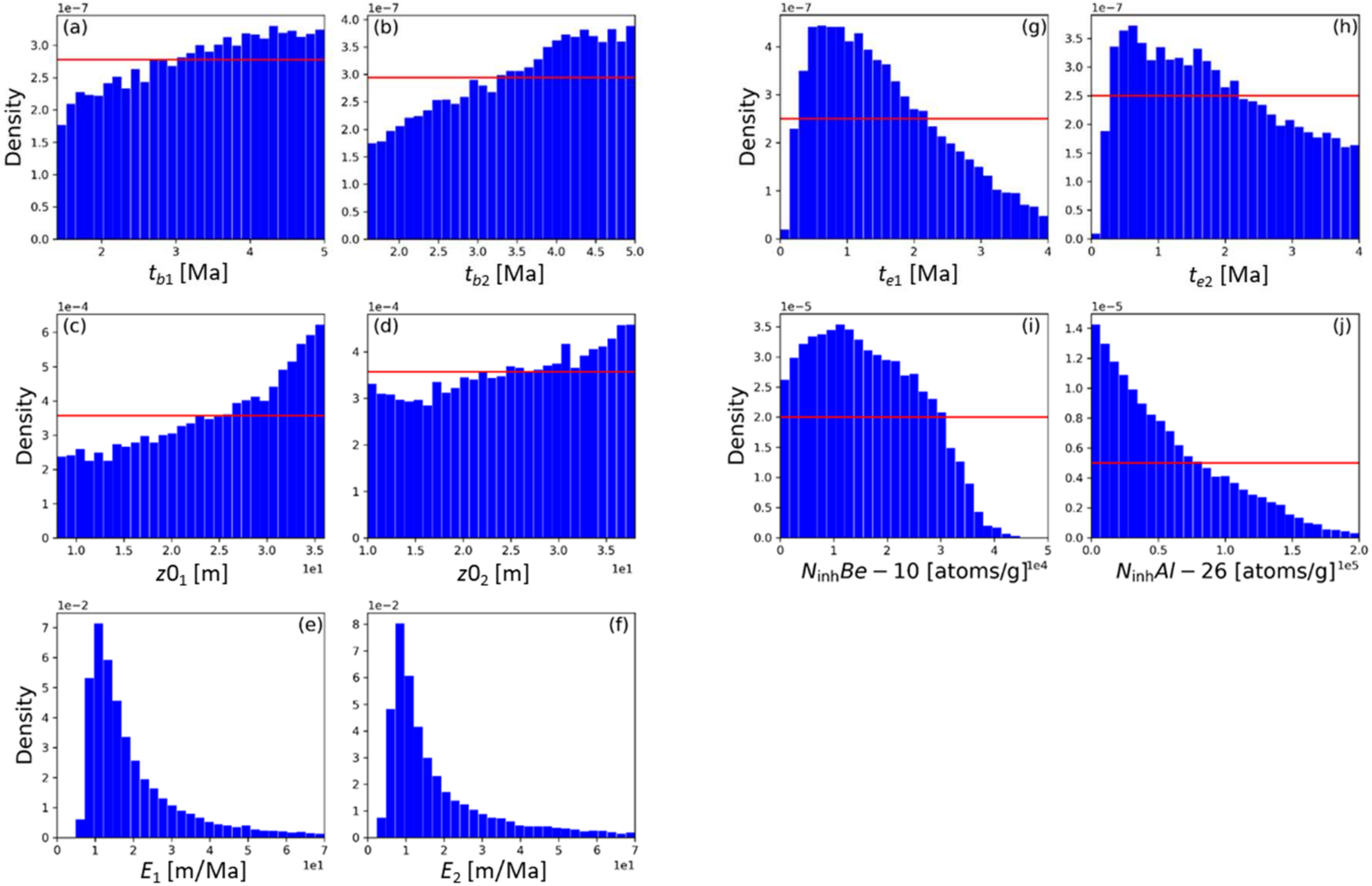
(a)
(b)
(c)
(d)
(e)
(f)
(g)
(h)
(i)
(j)
Density
t_{b1} [Ma]
t_{b2} [Ma]
$z0_1$ [m]
$z0_2$ [m]
E_1 [m/Ma]
E_2 [m/Ma]
t_{e1} [Ma]
t_{e2} [Ma]
$N_{inh}Be-10$ [atoms/g]
$N_{inh}Al-26$ [atoms/g]

Figure 10

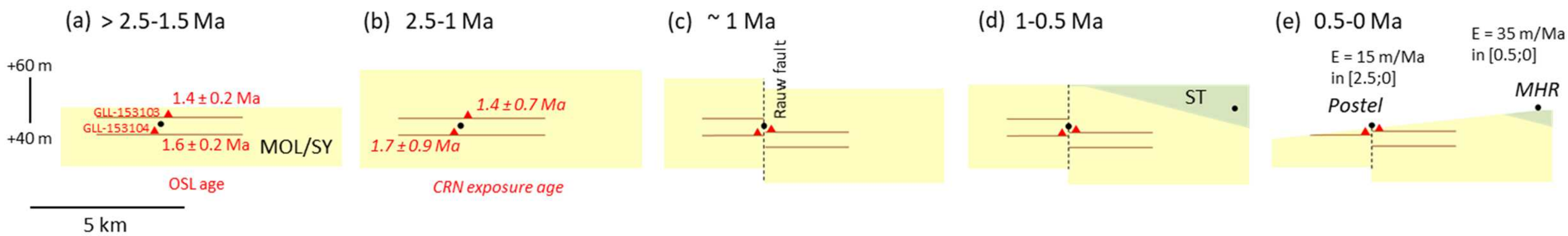
(a) > 2.5-1.5 Ma
+60 m
+40 m
1.4 ± 0.2 Ma
GLL-153103
GLL-153104
1.6 ± 0.2 Ma
MOL/SY
OSL age
5 km
(b) 2.5-1 Ma
1.4 ± 0.7 Ma
1.7 ± 0.9 Ma
CRN exposure age
(c) ~ 1 Ma
Rauw fault
(d) 1-0.5 Ma
ST
(e) 0.5-0 Ma
E = 15 m/Ma
in [2.5;0]
E = 35 m/Ma
in [0.5;0]
Postel
MHR

We declare that there is no conflict of interest for any of us (the authors).

On behalf of all authors,

Koen Beerten